



Climate changes in Anatolia across the late Eocene and the Eocene-Oligocene Transition: successive warming and cooling, aridification, and implications for the westward dispersal of Asian terrestrial mammals

5

Paul Botté¹, Alexis Licht¹, Anne-Lise Jourdan¹, Leny Montheil¹, François Demory¹, Mustafa Kaya², Faruk Ocakoğlu³, Mehmet Serkan Akkiaz⁴, Deniz İbilioglu⁴, Pauline Coster⁵, Grégoire Métais⁶, Benjamin Raynaud⁶ & K. Christopher Beard^{7,8}

¹ Aix Marseille University, CNRS, IRD, INRAE, CEREGE, Aix-en-Provence, France

10 ² Geological Institute, RWTH Aachen University, Aachen, Germany

³ Department of Geological Engineering, Eskeşehir Osmangazi University, Eskeşehir, Türkiye

⁴ Department of Geological Engineering, Kütahya Dumlupınar University, Kütahya, Türkiye

⁵ Réserve naturelle nationale géologique du Luberon, Unesco Global Geopark, Parc naturel régional du Luberon, Apt, France

15 ⁶ Centre de recherche en paléontologie - Paris (CR2P), Muséum national d'Histoire naturelle, Sorbonne Université, CNRS, Paris, France

⁷ Biodiversity Institute, University of Kansas, Lawrence, Kansas, USA

⁸ Department of Ecology and Evolutionary Biology, University of Kansas, Lawrence, Kansas, USA

Correspondence to: Paul Botté (botte@cerege.fr)

Abstract. The Eocene–Oligocene Transition (EOT dated at ~34 Ma) represents one of the most significant climatic shifts of 20 the Cenozoic, marking the transition from the last warmhouse state to a coolhouse state. This global cooling had major consequences for terrestrial ecosystems and was synchronous with the dispersal of numerous Asian mammalian clades towards western Europe. However, the terrestrial expression of the EOT exhibits strong regional heterogeneity. Consequently, its role in establishing dispersal corridors associated with the Grande Coupure remains unclear.

Here, we describe, date, and document the paleoenvironments of a continental sedimentary section from Balkanatolia, a 25 biogeographic province that most likely functioned as a critical stepping stone for the dispersal of Asian mammals toward western Europe. Our sedimentary record represents a fluvio-lacustrine system dated by magnetostratigraphy to the Priabonian and the lower Rupelian, including the Oi-1 glaciation (~33.65 Ma). Clumped isotopic analyses on pedogenic carbonates across our record show evidence for a Late Eocene Warming starting during the middle Priabonian (ca. 37 Ma), followed by a marked cooling event at the Eocene–Oligocene Glacial Maximum (EOGM). Stable isotopic data and sedimentary facies further 30 indicate that this complete interval is associated with a long-term aridification trend, starting during the Late Eocene warming and culminating at the EOT. Our results provide the first quantitative record of late Eocene warming on land, and our temperature estimates for the earliest Oligocene cooling are consistent with other Eurasian clumped-isotope records. These temperature shifts and associated aridification steps may have acted as contributing drivers of the late Eocene decline of



35 Balkanatolian endemic taxa and likely facilitated the westward expansion of Asia-derived mammals ultimately resulting in the colonization of western Europe.

1 Introduction

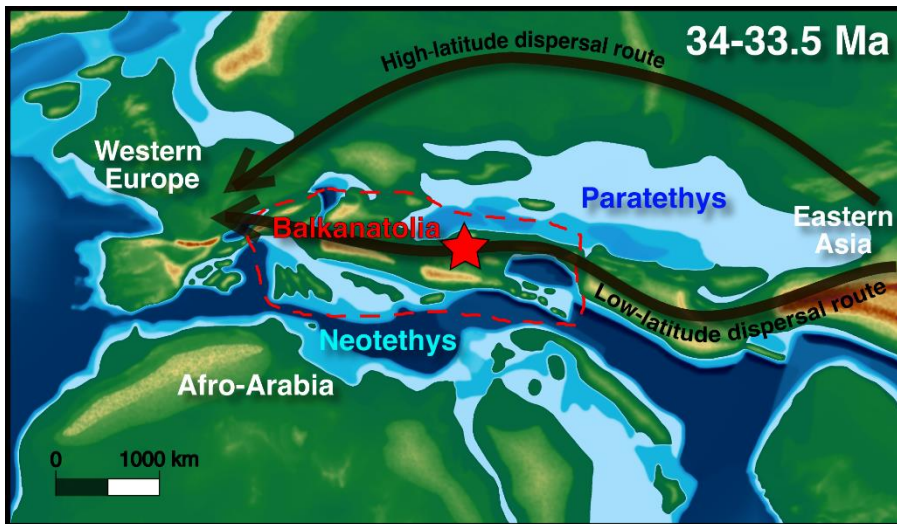
The Eocene-Oligocene Transition (EOT) is one of the main climatic events of the Cenozoic. It marks the transition between the last Warmhouse state of the Eocene to a Coolhouse state in the Oligocene (Westerhold et al., 2020). . The EOT is commonly 40 interpreted as a phase of accelerated climatic and biotic change, linked to an abrupt global drop in temperatures (Coxall and Pearson, 2007). This drop is primarily explained by a decline in atmospheric CO₂ concentrations and changes in oceanic gateways, which, in combination with orbital forcing, acted as triggers for the first major glaciation of Antarctica (DeConto and Pollard, 2003). Within the deep sea record, the EOT is defined by a homogeneous and marked positive excursion of δ¹⁸O from ~ 34.4 to 33.6 Ma (Katz et al., 2008; Hutchinson et al., 2021). The EOT is followed by the Early Oligocene Glacial 45 maximum (EOGM), dated from 33.65 to ~ 33.16 Ma. This latter corresponds to the peak of glacial expansion of the Oligocene associated with the major growth of the Antarctic ice sheet (Miller et al., 1991; Zachos et al., 1996; Hutchinson et al., 2021) While the EOT and the EOGM are well documented in marine records, their impact on land remains poorly understood. This is mainly due to the heterogeneous nature of its response: studies conducted so far show contrasting results regarding changes, or lack thereof, in seasonality, temperatures and the timing of these changes, if they occur. Pollen compilations have shown an 50 heterogeneous response of vegetation, especially in Eurasia where ecosystems show no, little, or a gradual shift to flora adapted to colder and more arid conditions (Pound and Saltzman, 2017). Stable and clumped isotope analysis of continental carbonates (such as pedogenic and lacustrine carbonates) provides an alternative insight into surface temperature and hydroclimate evolution and also underlines this heterogeneity. In North and South America, carbonate records indicate a cooling of temperatures and changes in seasonality, although with varying intensity and chronology (Kohn et al., 2015; Fan et al., 2017; 55 Antoine et al., 2021; Meijer et al., 2025). In Eurasia, the response to the EOT is much more heterogeneous. In Western Europe, geochemical proxies for weathering intensity in paleosols and stable isotopes in pedogenic carbonates indicate no significant changes of the paleoenvironment of climatic parameters such as the Mean Annual Temperature (MAT) or in seasonality in the Ebro Basin (Spain) and on the Isle of Wight (UK) (Sheldon et al., 2009; Sheldon et al., 2012). Other investigations on lacustrine carbonates, however, suggest a progressive shift toward more arid conditions, as observed in the Vistrenque Basin (France; 60 Semmani et al., 2024), with marked aridity peaks predating the EOT, such as in the Alès Basin (France; Lettéron et al., 2017). In addition, clumped isotope analyses of gastropod shells from the Hampshire Basin document a decrease in MAT by ~4-6°C across the EOT (Hren et al., 2013). Further east, in central Asia, Wang et al. (2020) found evidence for increasing aridification beginning prior to the EOT in the Tajik Basin (Tajikistan), based on carbon isotopes in pedogenic carbonates. Studies conducted in the Qaidam Basin (north-central Tibet) provide further evidence of dramatic climatic changes across the late 65 Eocene and the early Oligocene. Kent-Corson et al. (2009) documented a decrease in oxygen isotope values prior to the EOT,



interpreted as reflecting a decline in temperatures. By contrast, Sun et al. (2020) reported a positive shift in oxygen isotopes from carbonate mudstones spanning the late Eocene to the middle Oligocene, suggesting a long-term trend toward enhanced aridity. In the nearby Xining Basin (northeastern Tibet), Page et al. (2019) documented a temperature decrease of $\sim 20^{\circ}\text{C}$ occurring both prior to the EOT and during the EOGM. This decline is interpreted as resulting from both a shift in the 70 seasonality of carbonate formation and a decrease in surface temperatures, estimated at $\sim 9^{\circ}\text{C}$. In the Lanzhou Basin (northeasternmost Tibet), Li et al. (2016) reported a shift toward more positive oxygen isotope values in pedogenic carbonates after 33 Ma, suggesting the onset of aridification following the EOT.

This heterogeneous Eurasian response to global climate change at the EOT and EOGM has been traditionally linked to regional changes of atmospheric circulation impacting monsoonal rainfall in eastern Asia (Page et al., 2019), to the role of topography 75 dampening or enhancing global temperature and rainfalls, especially around the nascent Alps (Kocsis et al., 2014; Eronen et al., 2015), or to Paratethys sea retreat impacting specific areas of central Asia and the Middle East (Toumoulin et al., 2022). The variability and regionality of the climatic and vegetation response in Eurasia contrasts with the dramatic faunal changes that are witnessed at continental scale. In Mongolia, a major faunal turnover, known as the Mongolian Remodelling, is interpreted as a response to the climatic shift toward more arid conditions (Meng & McKenna, 1998). But the most important 80 faunal turnover spanning the late Priabonian and the earliest Oligocene is known as the “Grande Coupure” and corresponds to the extinction of 55% of European placental mammals (Weppe et al., 2023), coinciding with the arrival of Asia-derived mammals. Recent diversification modeling highlights the role of climate stress on western European taxa as a main driver for their decline, rather than competition with the arriving taxa (Weppe et al., 2023). Moreover, climate modeling suggests that the two proposed routes for dispersal (Fig. 1), via high latitudes in north-central Asia (Mennecart et al., 2021) and via mid 85 latitudes through Balkanatolia (Licht et al., 2022), were both significantly impacted by orbital and pCO₂ changes during the latest Eocene (Tardif et al., 2021). Climate change through the EOT might have favored the dispersal of Asia-derived taxa towards western Europe, though the ecosystem and climatic evolution is yet poorly documented in these two areas, where no terrestrial EOT record currently exists.

This study provides the first magnetostratigraphically dated continental section from Balkanatolia that records a hydroclimatic 90 response to the EOT, investigated through stable and clumped isotope analyses of pedogenic carbonates. We compare our hydroclimatic records with other Eurasian records to better characterize the regional climatic evolution around the EOT, and how it could have impacted the faunal dispersal occurring in the region.



95 **Figure 1: Paleogeographic map of Balkanatolia and the Neotethys realm at 34-33.5 Ma, modified from Montheil et al. (2025a).**
Arrows indicate the proposed dispersal routes of the “Grande Coupure” event. The studied location is shown with a red star.

2 Geological context

2.1 Balkanatolia

100 Balkanatolia is a semi-continuous strip of land extending from the Alpine region to the Lesser Caucasus (Licht et al., 2022) (Figure 2). It comprised various terranes of Laurasian (Tisza, Dacia, Rhodope, Strandja Massif and the Pontides) and Gondwanan (Alcapa, Greater Adria, Anatolide-Tauride, South Armenia) affinities that progressively accreted throughout the Cretaceous and the early Paleogene due to the northeastward motion of Afro-Arabia and Greater Adria and consequent closure of the Anatolian Neotethys and the Sava Ocean (Van Hinsbergen et al., 2020; Mueller et al., 2022; see Figure 2B).

105 During the Paleocene and Eocene, Balkanatolia consisted of large islands isolated from Afro-Arabia, Western Europe and Eastern Asia by the Paratethys to the north and west, the Neotethys to the south, and the Dobrujan, Valaisan and Carpathian seaways to the northeast (Barrier et al., 2018; Palcu and Krijgsman, 2022; Montheil et al., 2025a). This geographic isolation led to faunal endemism that prevailed until the Late Paleogene (Métais et al., 2018).

Tectonic activity and sea-level fluctuations created a dynamic landscape, often depicted as a mosaic of islands during the 110 Paleocene and Early Eocene (Popov et al., 2004). These fluctuations were caused by alternating phases of extension, thrusting, and shortening, resulting in submergence and emergence of the terranes (Van Hinsbergen et al., 2020). Between the Lutetian and Bartonian, the retreat of shallow seaways separating Balkanatolian islands enhanced land connectivity (Licht et al., 2022; Montheil et al., 2025a). As a result of renewed crustal shortening and sea level fall, terrestrial continuity with Laurasia was progressively re-established from the late Middle Eocene to Early Oligocene: first in the east via Anatolia and the Cimmerian



115 terranes (Barrier et al., 2018), then in the west through continental sediment infill of the Luda Kamchiya Trough, connecting to the Moesian Platform (Doglioni et al., 1996). The first arrival of Asia-derived taxa in Balkanatolia is dated to the Bartonian (40-38 Ma) and associated with the decline of Balkanatolian endemic taxa (Licht et al., 2022). This first wave of dispersal from Asia did not reach western Europe and Balkanatolia acted as a cul de sac (Métais et al., 2023). The first dispersal event of Asia-derived mammals to western Europe and passing through Balkanatolia is dated to the late Priabonian (mammalian biohorizon MP18-MP20; eg. 37-33.9 Ma) and involved anthracotheriidae, gelocidae and amphicyonidae (Metais et al., 2023).
120 Faunal exchanges through Balkanatolia appear to have reduced during the EOT and the EOGM in favor of the higher latitude routes, and resumed later during the Rupelian (See Figure 1; Mennecart et al., 2021; Metais et al., 2023).

2.2 The Cankiri Basin

125 Anatolia, as we know it today, is divided into the Pontides and the Anatolide-Taurides terranes, located in the northern and southern parts, respectively. The separation of these two terranes is marked by the Izmir-Ankara-Erzincan Suture (IAES). In central Anatolia, the Kırşehir Massif (also known as the Central Anatolian Crystalline Complex, CACC) is sandwiched between the Pontide and Anatolide-Taurides terranes. The Kırşehir Massif has been interpreted either as a former volcanic arc located between the Pontides and the Anatolide-Taurides (Lefebvre et al., 2013) or as the subducted and exhumed northern tip 130 of the Taurides (Van Hinsbergen et al., 2016). The exhumation of the CACC was followed by renewed contraction related to a Paleogene collision of the massif with the Pontides (Gülyüz et al., 2013).

The Çankırı Basin, at the northern edge of the CACC, is a sedimentary basin that can be subdivided in three main structural and stratigraphic units cropping out along its southern border, each reflecting distinct tectonic settings and depositional histories (Akgün et al., 2002, Kaymakçı et al., 2003) (Fig. 2C). The (1) *Çiçekdağı Belt*, represents the basin basement and 135 belongs to the crystalline core of the CACC. This unit corresponds to Cretaceous volcanic arc units (Lefebvre et al., 2013; Akgün et al., 2002) or is considered part of the Central Taurides (van Hinsbergen et al., 2020), which was accreted onto the Pontides during the collision with the Taurides (Licht et al., 2017). It is overlain by the (2) *Çankırı Basin Fill*, a Paleogene sequence filled with shallow marine to continental deposits (Akgün et al., 2002). This unit records alternating episodes of marine and lacustrine transgression and regression throughout the Paleogene. The lower part consists of a Paleocene-Eocene 140 regressive sequence, transitioning from flysch to molasse, and later overlain by nummulitic limestones. From the Middle Eocene to the Oligocene, the sea progressively retreated, giving way to predominantly more continental red clastics, intercalated with and eventually overlain by Oligocene evaporites (Kaymakçı et al., 2003). The third unit, referred to as the (3) *cover series*, overlies the Cretaceous–Paleogene deposits and began to accumulate during the Early Miocene with fluvio-lacustrine sediments alternating with evaporitic layers, continuing up to the Plio-Quaternary (Kaymakçı et al., 2003; Akgün et 145 al., 2002).

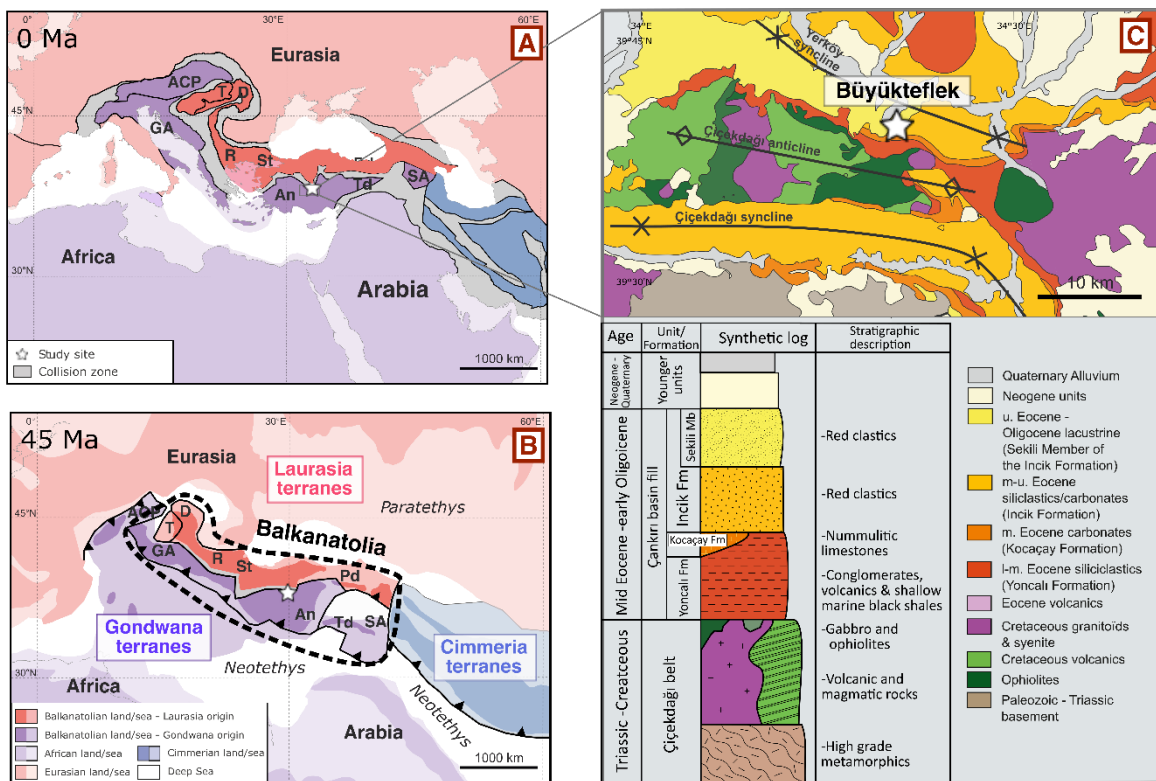
During most of the Eocene, the basin was bounded by the sea: the northern part of Çankırı corresponded to a deep-sea environment, which was tectonically active due to its proximity to the IAES zone, while the southern part corresponded to a partly shallow marine to continental deltaic environment, which was relatively tectonically quiescent (reference here). During



the late Eocene (Priabonian), marine deposition had ceased, and the basin had lost its connection to the sea, evolving into a
 150 large, closed lacustrine system (Campbell et al., 2025).

Our study site is located in the Çiçekdağı area (Fig. 2C). In the area, the *Çiçekdağı Belt* crops out along the Çiçekdağı anticline, which separates the Çiçekdağı Syncline and the Yerköy Syncline, located to the south and north of the Çiçekdağı area, respectively, where Paleogene deposits of the Çankırı Basin fill are exposed (Gülyüz et al., 2013; Licht et al. 2022).

The sedimentary sequence begins with the Yoncalı Formation, which contains conglomerates with volcanic clasts and lignites
 155 (Lichte et al., 2022). It is overlain by the Late Lutetian–Early Priabonian marine limestones of the Kocaçay Formation, which are rich in nummulites (Akgün et al., 2002; Gülyüz et al., 2013; Licht et al., 2022). Above these beds, lie the continental deposits of the Incik Formation, where fossils of Asian mammals from the Brontotheriidae and Hyracodontidae families have recently been discovered (Licht et al., 2022). These are then overlain by lacustrine deposits including marls, gypsum beds, and tuffs, known as the Sekili Member of the Incik Formation (Fig. 2C).



160

Figure 2: (A) Current structural overview of the Balkanatolian terranes. ST (Standja Massif), An-TD (Anatolide-Tauride), D (Dacia, SA South Armenia), Pd (Pontides), R (Rhodope), ACP (Alcapa), T (Tisza), GA (Greater Adria). (B) Middle Eocene structural overview of Balkanatolia. The star indicates the studied locality of Büyükteflek. (C) Simplified geological map of the Çiçekdağı Basin, with the synthetic stratigraphic log and the different basin units. (maps modified from Montheil et al., 2025b)



2.3 The Büyüktflek section

Our study section is located within the Yerköy Syncline, near the village of Büyüktflek (See Fig. 2C; See Supplementary Figures Fig. S1), and spans the Incik Formation and the Sekili Member. In this area, the Incik Formation is represented by red beds, sandstones, conglomerates, and pedogenic carbonates. In the upper part of the section, the base of the Sekili Member is marked by thick conglomeratic units and sandstone bodies containing reworked carbonate clasts and invertebrate fossils derived from the upper Kocaçay Formation, where caliche horizons are commonly developed (Licht et al., 2022). This section has been previously studied by Gülyüz et al. (2013) and Licht et al. (2022). The latter work provided improved constraints on the basal part of the section, assigning a Priabonian age based on marine microfossils (ostracod and planktonic foraminifera) assemblage within the uppermost beds of the Kocaçay Formation. The upper part of the section, covering the Sekili Member, was dated using U–Pb analyses of interbedded tuff layers, yielding ages of 32.1 ± 1.1 Ma and 32.6 ± 1.1 Ma and was correlated with the reversed polarity chron C12r (early Rupelian) based on magnetostratigraphic data. The lower part of the section, extending from the Incik Formation to the base of the Sekili Member, was insufficiently sampled, preventing a precise assignment by magnetostratigraphy within the Priabonian and the early Rupelian. Given the age constraints for the lower (Priabonian) and the upper (Rupelian) parts, the section should cover the EOT.

3 Methods

3.1 Sedimentary logging

We measured and logged a 195 m section spanning the Incik Formation and the Sekili Member at ~ 50 cm resolution, located 185 at the Büyüktflek locality of Licht et al. (2022) (See Supplementary Figures Fig. S1 for the overall picture of the Büyüktflek section). Our detailed stratigraphic log started at the level 150m of the one of Licht et al. (2022), ending at the level 345m. The sedimentary facies of these sections were characterized and classified into 6 distinct lithofacies, adapted on the classification of Miall (2013). Pictures of the sedimentary facies are displayed in Fig. 3, microphotographs and complementary pictures are available in the Supplementary figures Fig. S2.

190 3.2 X-Ray diffraction (XRD)

25 carbonate samples were collected all along the section and consist of nodules or blocks from continuous massive, carbonated layers. All the samples were reduced to powder with a Dremel, and filtered with a 160 μm sieve. The mineralogy of the carbonate samples was characterized using an X'Pert Pro MPD X-ray diffractometer (Malvern Panalytical), equipped with a cobalt X-ray tube (wavelength $\lambda = 1.79$ Å), operating at 40 kV and 40 mA. Detailed procedure can be found in Couturier et al.



195 (2025). Sample powder was deposited onto low-background Silicium (Si) plates. The powders were homogenized using drops of ethanol and allowed to dry. During analysis, samples were rotated at 15 rpm to improve measurement quality. XRD scans were conducted over a 20 range from 34° to 38°, with a step size of 0.026°. Each scan lasted 10 minutes, allowing for the identification of carbonate mineral phases based on their primary diffraction peaks.

3.3 Magnetostratigraphy

200 For the magnetostratigraphic study, 110 rock samples were collected using a portable electric drill (core diameter of 1 inch) and oriented with a magnetic compass. Samples were retrieved from red clastic layers ranging from clay to silt grain size and from pedogenic carbonates (from nodules to well-developed caliches) developed on silty sandstones or red clastics. We also, collected 9 oriented blocks in clay rocks that when rocks were too soft to be drilled.

205 Natural Remanent magnetization and either its stepwise alternating field (AF) demagnetization with field increments of 5 mT from 0 to 70 mT or its stepwise thermal (TH) demagnetization with temperature increments of 20°C, 30°C, 40°C or 50°C from room temperature (~20°C) up to 660°C were measured with the Superconducting Rock Magnetometer SRM760R (2G enterprises) of CEREGE (Aix-Marseille University). Remanent signal from some clay samples was resistant to alternating field (AF) demagnetization and consequently required thermal demagnetization.

210 89 samples were demagnetized using alternating field (AF) demagnetization, and 17 samples were subjected to thermal demagnetization. Among these, 14 samples were analyzed using both methods. Data were plotted in orthogonal diagrams (Zijderveld, 1967) and stereographic projection and interpreted using the PuffinPplot software (Lurcock and Wilson, 2012). ChRM directions were then calculated using the principal component analysis of Kirschvink (1980). Samples exhibiting low magnetic intensity or lacked a coherent directional trend, likely reflecting local noise rather than a primary signal, were excluded from the dataset.

215 3.4 Stable and clumped Isotopes

220 24 carbonate sample powders identified as pure calcite from XRD, and one composed of approximately equal proportions of calcite and dolomite, were selected for stable isotopic analysis. The samples were analysed on a Thermo 253+ mass spectrometer attached to a Thermo Kiel IV device, run under the Qtegra™ software wnd in Dual Inlet mode at CEREGE. Sample powder corresponding to around 80-120 µg of pure carbonate was loaded into glass vials and placed on a carousel along with international standards (IAEA-603, NBS18) and laboratory standards (BDH and VIA-1, which are made of pure calcite) in the Kiel over held at 70°C. After each vial is in turn put under vacuum, the powder reacts with 2 to 3 drops of 105% phosphoric acid at 70°C to produce CO₂ for analysis. The released CO₂ is then trapped and cleaned via a series of cryo-traps, and finally sent to the Thermo 253+ mass spectrometer for measurements of the oxygen and carbon isotopes values. Isotopic values are reported relative to IAEA-603 international standards in the V-PDB reference frame.



225 14 of these samples were selected for clumped isotope analysis and were treated overnight with 3-8% NaOCl, rinsed and
centrifuged 4 times and dried with a freeze-drier, to remove nitrate contamination (Fiebig et al., 2024). The samples were then
analysed at CEREGE on the same previously described system. Details about the clumped isotope procedure at CEREGE are
given in Supplementary Text S1. Briefly, primary standards (ETH-1 to -4), secondary standards and unknown sample powders
were loaded into the glass vials and placed on the carousel of the Kiel oven still held at 70°C. The procedure is similar to the
230 one described above for stable isotope measurement with the exception of an additional step of cryotrapping involving a trap
filled with a Porapak molecular sieve, held at -20°C by a Peltier system. The resulting purified CO₂ gas is transferred to the
253+, where extra faraday cups will allow the measurement of clumped isotopes (m/z 47, 48, 49) on top of carbon and oxygen
isotopes (m/z 44, 45, 46) and pressure baseline corrections (m/z 47.5 and 48.5).

Baseline-corrected δ data are screened with an in-house Matlab script for statistical outliers and are then translated into $\delta^{18}\text{O}$,
235 $\delta^{13}\text{C}$ and Δ^{47} projected to the Intercarb-Carbon Dioxide Equilibrium Scale (I-CDES90; Bernasconi et al., 2021) using
D47crunch (Daëron, 2021), pooling over data from all sessions of the dataset. In total, we run 10 to 20 replicates per unknown
sample spread over 28 sessions, with an inter-session repeatability of 30 ppm in Δ^{47} for all replicates (unknown and standards).
Paleotemperatures are calculated using the unified $\Delta^{47}\text{-T}$ calibration of Anderson et al. (2021). Uncertainties around
temperature estimates are provided with and without propagating intersession-related uncertainty (difference of ± 1 to 2 °C at
240 2s).

Note that to test the reproducibility of our results and the impact of the NaOCl pre-treatment, three samples were divided into
two aliquots: one with pre-treatment, and one without. We found no statistical difference between pre-treated and non-treated
samples.

Data presented in the manuscript are only from pre-treated samples. Raw data for unknown samples and standards are provided
245 together with interpreted data, to allow possible future reprocessing of Δ^{47} values and paleo-temperature estimates, in
Supplementary table 4.

250

255



4 Results

260 4.1 Sedimentology of the Büyükteflek section

The lower part of the studied section (from ~100 to 263 m) is characterized by three distinct sedimentary facies (Table 1). The first facies (Fmp; see Fig. 3B,C,D) consists of clayey to silty red beds, generally massive in structure, and occasionally exhibiting discontinuous planar laminations. These deposits may contain root traces and reduced mottling. Above level 240

265 m, they display more developed pedogenic features, including small carbonate nodules to well-developed caliche horizons. X-ray diffraction (XRD) analysis indicates that all carbonate samples from these beds are composed exclusively of calcite. The second facies (St; see Fig. 3G,H) is composed of channelized, trough cross-bedded sandstones, with grain-size ranging from very fine to medium sand. Some beds contain thin layers of gravel or pebbles. The fossiliferous horizon described by Licht et al. (2022), containing Brontotheriidae (*Embolotherium aff. andrewsi*) and Hyracodontidae (*Prohyracodon* sp.), occurs at approximately the 215-meter level within these facies. The third facies (Sm; see Fig. 3D) consists of structureless greenish

270 medium to coarse sandstones, containing isolated clasts ranging in size from gravel to approximately 2 cm. The three facies Fmp-St-Sm are grouped under Facies Association FA1 (Table 2).

The level at 263 meters is marked by a field-identifiable surface, corresponding to a channelized erosional surface developed above a well-developed caliche. This hiatus was interpreted by Licht et al. (2022) as the boundary between the Incik Formation and the Sekili Member (Hiatus 1 on Fig. 4). From 263 m to 292 m, the facies consist of channelized sandstones (St) and

275 pedogenized clay to silty red beds (Fmp). This interval marks the appearance of three new facies. The first one (Smp; see Fig. 3A,E,F) consists of reddish to pinkish, massive, very fine- to fine-grained sands. These beds are strongly pedogenized and feature carbonate nodules, well-developed caliche horizons or diffuse carbonate. The second facies (Gmm; see Fig. 3G), which is coarser, is composed of massive, matrix-supported conglomerates with a sandy matrix, containing clasts ranging from 1 mm to 5–10 cm and exhibiting weak normal grading. Some of these conglomerates include reworked Nummulites, probably

280 derived from underlying marine deposits. The last facies (Gmc; see Fig. 3B,E,G) consists of clast-supported conglomerates with a sandy matrix, containing imbricated clasts ranging from 1 mm to 5–20 cm, and may also contain reworked nummulites.

These three new facies, together with the channelized sandstone Smp-St-Gmm-Gmc are grouped under Facies Association FA2 (Table 2). X-ray diffraction analysis indicates that the nodules found at these depths contain only calcite.

At 292 meters, a second unconformity is observed, marked by the development of a 2–4 m thick caliche (Hiatus 2; see Fig. 4).

285 This paleosol is the thickest of the section and forms a topographic feature that can be tracked over hundreds of meters (Fig. 3A). Five facies are present from this unconformity up to the top of the logged section in this study (level 355 m). These include the same channelized sandstones (St), along with pedogenized red beds assigned to the Fmp facies. The Smp facies is also identified, which is particularly abundant in this part of the section. X-ray diffraction analysis shows that carbonate in these beds may contain either calcite (from 292 m to 325 m) or dolomite (from 302 m to 355 m). In addition, the two 290 conglomerate facies, Gmm and Gmc, are present within this part of the section. This interval of the log includes both facies associations FA1 and FA2.



Facies	Grain Size	Bed Thickness	Description	Pedogenic Features	Interpretation	References for the interpretation
Fmp	Clay to silt	10 cm to 1 m	Massive red beds, occasionally displaying discontinuous planar laminations.	Root traces, reduced mottles, carbonate nodules to well-developed caliche horizons.	Overbank deposits in floodplain or delta plain environments.	Bhattacharya (2010); Miall (2010); Leeder (2016)
St	Very fine to medium sand	10 to 50 cm	Trough cross-bedded sandstones organized in cosets. Some layers contain thin beds of gravels or pebbles.	None	Sand bars in river channels, delta distributary channels or at delta mouth bars	Bhattacharya (2010); Miall (2010)
Sm	Medium sand to gravel	10 to 50 cm	Structureless greenish sandstones containing gravel-sized clasts up to 2 cm. sometimes carbonated.	None	Sediment gravity-flow deposits.	Miall (2010)
Smp	Very fine to fine sand	5 to 20 cm (sets)	Reddish to pinkish massive sandstones, which may either be strongly pedogenized with well-developed caliche horizons predominantly composed of calcite) or exhibit diffuse carbonate cementation (predominantly composed of dolomite).	Pedogenic carbonate nodules to well-developed caliche horizons.	Sand bars in river channels, delta distributary channels, delta mouth bars, or distal fan gravity flow deposits that have undergone later emersion and pedogenesis	Leeder (2016); Miall (2010)



Gmm	Conglomerate (matrix-supported)	2 to 5 m (to confirm)	Massive, matrix-supported conglomerates with a sandy matrix, occasionally displaying cross-bedding. Clasts range from 1 mm to 5–10 cm and exhibit weak normal grading. These deposits occasionally contain reworked <i>Nummulites</i> derived from underlying marine beds	Occasional well-developed caliches	High-strength cohesive debris-flow deposits.	Miall (2010)
Gmc	Conglomerate (clast-supported)	2 to 5 m (to confirm)	Clast-supported conglomerates with a sandy matrix, containing imbricated clasts ranging from 1 mm to 5–20 cm. May also contain reworked <i>Nummulites</i> .	None	Pseudoplastic debris flows (inertial bedload, turbulent flow).	Miall (2010)

295 **Table 1: Sedimentary facies of the Büyükteflek section**

Facies Association Name	Facies	Interpretation	Sources/References
FA1	Fmp-St-Sm	Floodplain/alluvial plain	Miall (2010); Leeder(2016);
FA2	Smp-St-Gmm-Gmc	Lacustrine fan-delta	Miall (2010); Renaut and Gierlowski-Kordesch (2010)

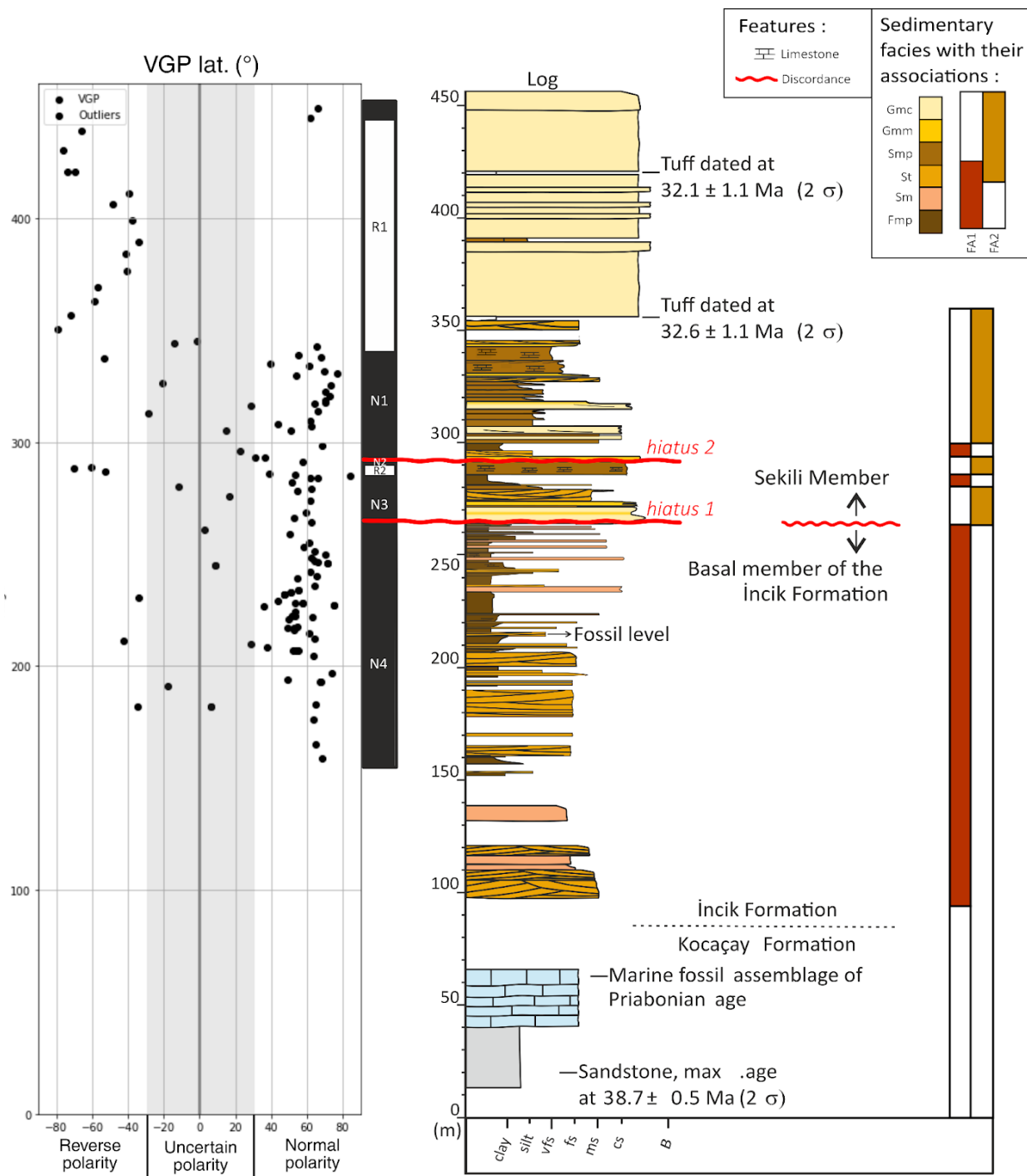
Table 2 : Facies associations of the Büyükteflek section

300

305



Figure 3 : Examples of sedimentary facies described in Table 1. (A) Well-developed caliche (facies Smp); Hiatus 2, marked by red dotted lines, corresponds to the stratigraphic level at 292 m; hammer for scale. **(B)** Well-developed caliche (facies Fmp), eroded at the top by channelized conglomerates (facies Gmc); this surface corresponds to Hiatus 1 at 263 m; hammer for scale. **(C)** Massive clayish red beds (facies Fmp); hammer for scale. **(D)** Massive greenish sandstones containing gravel-sized clasts up to 2 cm (facies Sm), overlying red beds (facies Fmp); knife for scale. **(E)** Clast-supported conglomerates overlying caliche developed in sandstones (facies Smp); hammer for scale. **(F)** Massive sandstone with diffuse carbonate development (facies Smp); knife for scale. **(G)** Alternation of matrix-supported (facies Gmm) clast-supported conglomerates (facies Gmc) and the channelized sandstones (facies St); Leny Montheil (180 cm) for scale. **(H)** Trough cross-bedded sandstones (facies St); hammer for scale.



315 **Figure 4:** Stratigraphic log of the Büyükteflek section. Colour coding illustrates the different facies and facies associations. The VGP latitude diagram shows the paleomagnetic data and the corresponding magnetozones (R1, N1, N2, R2, N3, N4).



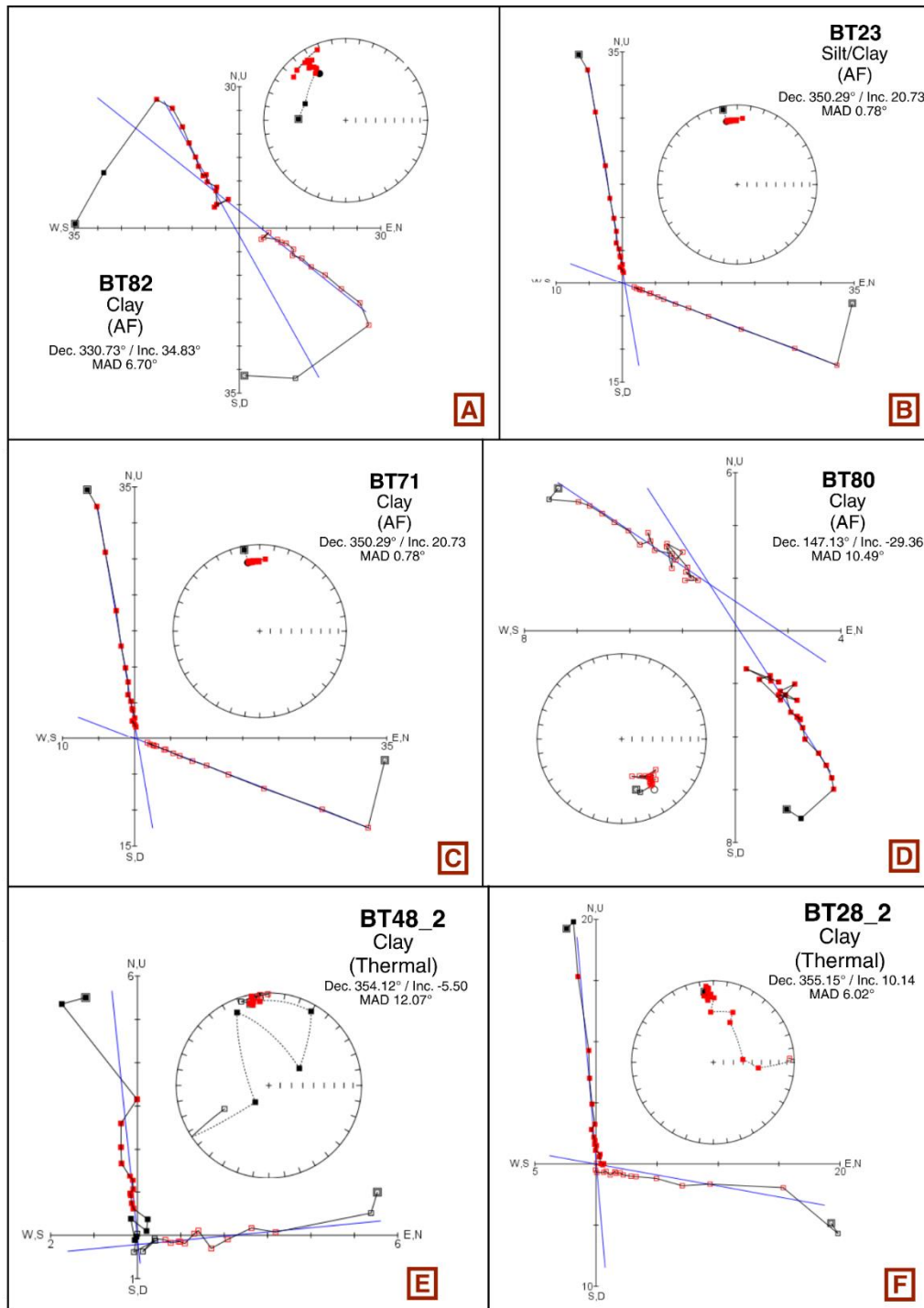
4.2 Magnetostratigraphy of the Büyükteflek section

320 The magnetostratigraphic data presented here complement the work of Licht et al. (2022) on the same section. Magnetic intensity measurements revealed that clay samples generally exhibited weaker intensities, ranging from 6.9×10^{-4} to 1.5×10^{-1} A/m, while coarser samples, from silt to fine sand, displayed higher intensities, ranging from 1.5×10^{-2} to 8.9×10^{-1} A/m. Some samples showed evidence of a viscous component in both fine and coarse grain sizes (e.g., BT82, Fig. 5A). For the silt to fine sand fraction, demagnetization typically revealed a stable decay toward the origin (e.g., BT23 Fig. 5B). Similarly, several clay samples also display a consistent decay toward the origin, though often accompanied by a higher degree of noise (e.g., BT71, BT80, Fig. 5C,D). Thermal demagnetization of selected clay samples was carried out between 120°C and 500°C (e.g., BT48_2, BT28_2, Fig. 5E, F; See Supplementary table 1 and Supplementary data 1).

325 These thermal demagnetization results suggest the presence of both magnetite and hematite, with sometimes the unblocking temperature ranges supporting their coexistence. Zijderveld diagrams for these samples typically show a single-component decay, indicating the presence of a stable Characteristic Remanent Magnetization (ChRM) (see representative example in Fig. 5).

330 More samples recorded a primary normal geomagnetic polarity than a reverse geomagnetic polarity. This result is in good agreement with the investigated time interval characterized by a predominance of long lasting normal polarity chronos. To complete the geomagnetic polarity record, we added the magnetostratigraphic dataset from Licht et al. (2022), which covers 335 the upper part of the section and includes a higher proportion of reversely magnetized samples attributed to Chron C12r.

340 Reversal tests and calculations of reversal angles were performed using both custom Python scripts and the Paleomagnetism.org platform. The reversal test yielded positive results. While normal-polarity samples show consistent and well-clustered directions, reverse-polarity samples are more scattered, likely due to the limited number of data points. Nonetheless, the antipodal relationship between the normal and reversed directions supports the interpretation of a primary ChRM (See Supplementary Figures Fig. S5). Furthermore, samples containing both magnetite and hematite exhibit a single-component magnetization, suggesting that hematite recorded the ambient magnetic field during or shortly after deposition, rather than during later mineralogical alteration. This supports the interpretation of the ChRM as a relatively primary signal. Five distinct magnetic chronos have been identified within the Sekili Member interval of the studied section. These chronos are 345 defined based on the presence of at least three consecutive, reliable samples exhibiting consistent magnetic polarity. In contrast, the lower part of the section, corresponding to the Incik Formation, displays less well-defined magnetic chronos, likely due to lower sampling resolution or increased diagenetic overprinting. However, the dominance of normal polarity intervals in this portion of the section led us to interpret it as representing a normal chron.



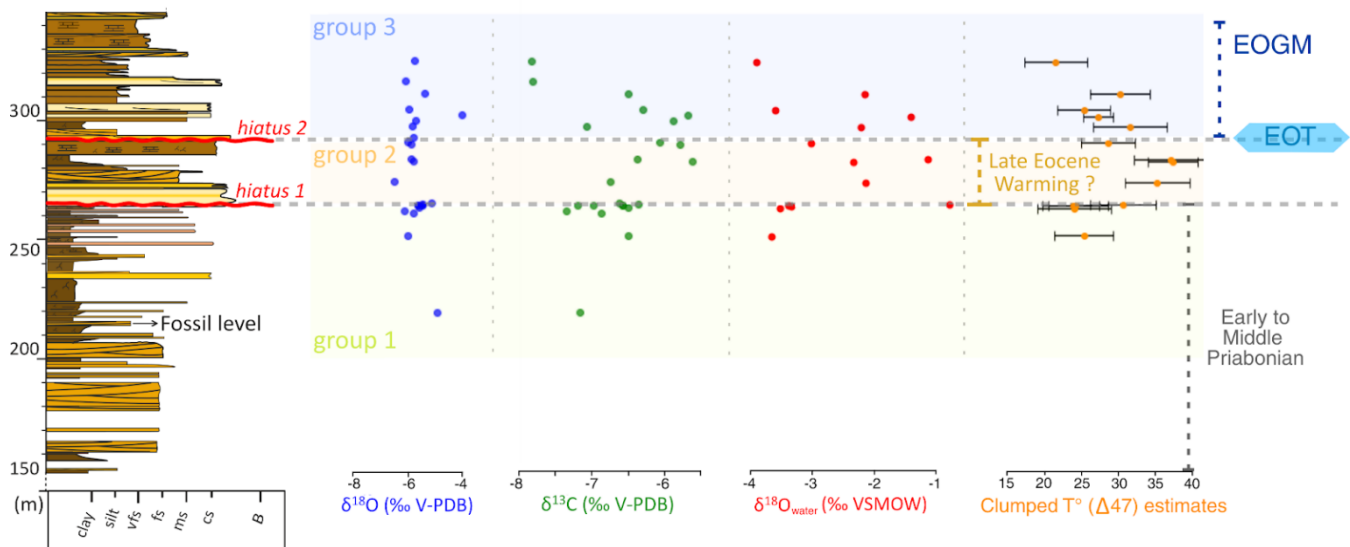
350 **Figure 5: Representative intensity plots and Zijderveld diagrams obtained after Alternating Field (AF) and Thermal demagnetization.**



4.3 Stable and Clumped isotopes

The stable isotope composition of calcite samples ranges from $-6.5\text{\textperthousand}$ to $-5.1\text{\textperthousand}$ for $\delta^{18}\text{O}$ (on average: $-5.7\text{\textperthousand}$ V-PDB) and from $-7.8\text{\textperthousand}$ to $-5.2\text{\textperthousand}$ for $\delta^{13}\text{C}$ (\textperthousand V-PDB). Calcite $\delta^{18}\text{O}$ values do not exhibit any clear stratigraphic trend throughout the section. In contrast, $\delta^{13}\text{C}$ values for calcite are slightly more variable. Below Hiatus 1, $\delta^{13}\text{C}$ values average $-6.8\text{\textperthousand}$. Between Hiatus 1 and Hiatus 2, these values increase slightly, with a mean of $-6.1\text{\textperthousand}$. Above Hiatus 2, $\delta^{13}\text{C}$ values display a decreasing trend, ranging from $-5.9\text{\textperthousand}$ to $-7.8\text{\textperthousand}$ with an average value of $-6.9\text{\textperthousand}$. Among the samples above Hiatus 2, one contains both calcite and dolomite in approximately equal proportions. Given its comparable clumped isotopic values to those of other samples, it was retained in the results and discussion (See Supplementary Table 3). Clumped isotope-derived temperatures ($\Delta 47$) from pedogenic calcite carbonates fall within the range of Earth's surface temperatures ($<40^\circ\text{C}$). The $\Delta 47$ results can be divided into three distinct groups. The first group (all samples below hiatus 1, but the very last sample; 4 samples in total) shows relatively stable values, with a mean temperature of $24.4^\circ\text{C} \pm 0.7$ (2s). A significant increase in surface temperature is observed in the second group, corresponding to the last sample below hiatus 1 and all the samples situated between Hiatus 1 and Hiatus 2 (5 samples in total). This interval yields a higher and relatively consistent mean temperature of $34^\circ\text{C} \pm 3.5$ (2s), representing a $\sim 9^\circ\text{C}$ increase compared to the interval below Hiatus 1. Then the third group shows a decreasing trend in temperatures. The third group (5 samples), located above Hiatus 2, displays decreasing temperatures of $\sim 7\text{--}8^\circ\text{C}$. This group yields a mean $\Delta 47$ -derived temperature of $27.4^\circ\text{C} \pm 3.6$ (2s), with respectively the highest to the lowest values from $31.9 \pm 5^\circ\text{C}$ to $21.6^\circ\text{C} \pm 4.2^\circ\text{C}$. Clumped isotopic results from the sample with a mixture of dolomite and calcite sample yield similar $\Delta 47$ values than for pure calcite samples of the same interval, suggesting that the CO_2 extracted during the acid reaction at 70°C is prominently calcitic (e.g. Li et al., 2023). The exclusion of the sample from our dataset does not alter the average temperature of the interval (e.g. 27.5 ± 4.1 2s without the sample instead of 27.4 ± 3.6 2s with it). Student's *t*-tests were performed between the first and second groups, and between the second and third groups. The three groups show statistically significant differences. The comparison between Group 1 and Group 2 yielded a *p*-value of 0.005 and an effect size (Cohen's *d*) of $|d| = 3.33$, indicating a strong statistical difference between these two groups. Similarly, the comparison between Group 2 and Group 3 produced a *t*-test *p*-value of 0.030 and an effect size of $|d| = 1.668$, also suggesting a substantial difference between the (See supplementary table 4).

Based on clumped and stable isotope data, $\delta^{18}\text{O}_{\text{water}}$ values (V-SMOW) have been reconstructed according to Kim and O'Neil (1997) recalculation (See Fig. 6). These values can be divided into three groups, consistent with the grouping defined from clumped isotope temperatures. Group 1 displays a mean $\delta^{18}\text{O}_{\text{water}}$ value of $-3.6\text{\textperthousand}$ (V-SMOW). A marked increase is observed at the final sample just before Hiatus 1, with Group 2 showing a mean value of $-1.9\text{\textperthousand}$. This is followed by a slight decrease in Group 3, which exhibits a mean $\delta^{18}\text{O}_{\text{water}}$ value of $-2.7\text{\textperthousand}$ (See Supplementary table 5).



385 **Figure 6:** Scaled stratigraphic log highlighting the pedogenic carbonate sampling interval. From left to right are plotted $\delta^{18}\text{O}$, $\delta^{13}\text{C}$, $\delta^{18}\text{O}_{\text{water}}$, and $\Delta 47$ values from pedogenic carbonates. Coloured fields (light green, light orange, light blue) indicate distinct groups, interpreted as reflecting differences separated by the hiatuses. Horizontal grey dotted lines delineate the hiatus 1 and hiatus 2.

5 Discussion

390 5.1 Refining the Age of the Büyükteflek Section Across the Eocene–Oligocene Transition

The paleomagnetic record of the Büyükteflek section was established by integrating the chronos identified here with the magnetostratigraphic framework published by Licht et al. (2022). A total of six distinct chronos were recognized, comprising four normal polarity intervals and two reversed polarity intervals. The basal portion of the section could not be confidently correlated with a specific chronon due to the scarcity of reversed-polarity samples, suggesting that one or more magnetic reversals 395 may have gone unrecorded or unsampled in this lower interval (See Fig. 7). Magnetozones were identified and correlated with the Geologic Time Scale 2020 (Gradstein et al., 2020).

Following the work of Licht et al. (2022), we initially correlated the uppermost reversed-polarity magnetozone (R1) with Chron C12r (33.21–30.98 Ma), and the underlying normal polarity magnetozone (N1) with Chron C13n (33.73–33.31 Ma) based on the age of two volcanic layers dated in the section at 355m and 420m. The limestone beds beneath our lowermost 400 paleomagnetic sample have been dated by biostratigraphy to the Priabonian stage (Licht et al., 2022), providing a maximum age of 37.71 Ma. This dating is strengthened by the sandstones underlying the limestone beds, which yield a U-Pb maximum depositional age of 38.7 ± 0.5 Ma (2σ) (Licht et al., 2022). The overlying strata, which include the normal polarity magnetozone N4, therefore postdate this age. This interval contains mostly normal polarity samples, with only a few isolated reversed ones, suggesting that magnetic reversals may not have been preserved due to erosion, non-deposition, or limited sampling resolution.



405 Several correlation scenarios were considered using these constraints (See Supplementary Figures Fig. S2 and Fig. S3), and we retained the interpretation that yields the most stable sediment accumulation rates through the section (See Supplementary Table 2). Just below Hiatus 2, the normal polarity magnetozone N2 is correlated with Chron C16n.1n (35.72–35.58 Ma), the reversed magnetozone R2 with Chron C16n.1r (35.77–35.72 Ma), and the underlying normal magnetozone N3 with Chron C16n.2n (36.35–35.77 Ma). The N4 interval is correlated with the mid-part of Chron C17n.2n to Chron C17n.1n (~37.71–
410 36.57 Ma).

This magnetostratigraphic framework allows for temporal subdivision of the Büyükteflek section. The basal unit, below the first unconformity, corresponds to the early to middle Priabonian. The layer at 215 m, which yielded fossils of Brontotheriidae (*Embolotherium* aff. *andrewsi*) and Hyracodontidae (*Prohyracodon* sp.), is correlated with the interval ranging from the mid-part of Chron C17n.2n to Chron C17n.1n. This magnetostratigraphic position constrains the age of the fossil-bearing horizon
415 to approximately 37.71 to 36.57 Ma (the Priabonian part of C17n). The interval between the two unconformities spans a time frame around ~36 Ma and corresponds to Chrons C16n.2n, C16n.1r, and C16n.1n. Based on the average accumulation rate across the section, this interval is expected to last around 675 kyr. The upper part of the section, above the second unconformity, is attributed to chron C13n and C12r. Chron C13n coincides with the Eocene Oligocene Glacial Maximum (EOGM; Hutchinson et al., 2021), while the uppermost part corresponds to the transition to the warmer times of the Oligocene.

420

425

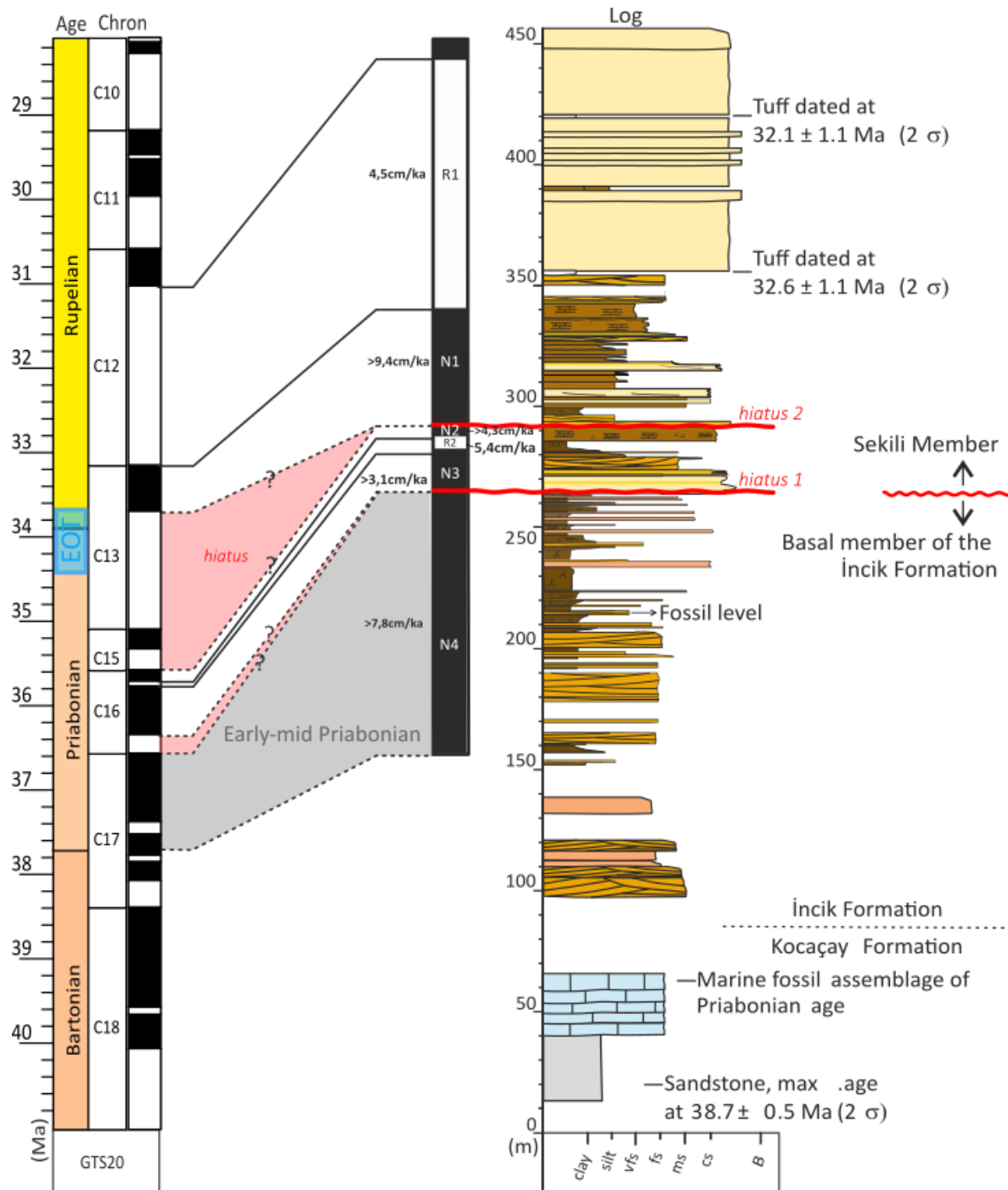


Figure 7: Stratigraphic log of the Büyükteflek section showing the magnetostratigraphic correlation with associated accumulation rate (R1;R2) and minimum accumulation rates (N1;N2;N3;N4), calibrated with the Paleogene Geomagnetic Polarity Time Scale (Gradstein et al., 2020).



5.2 Evolution of the depositional system and origin of the unconformities

435 Previous work by Gülyüz et al. (2013), suggested that episodes of folding, thrusting, and uplift along the Çicekdağı anticline, located directly to the south of our section, began between ~38 and 35 Ma. They also identified a reversal of the direction of paleocurrents from predominantly southward to northward flow direction within the Sekili Member, suggesting a local reorganization of paleodrainages. It is thus very likely that the two unconformities recorded in our section are at least partly related to on-going uplift and deformation of the southern margin of the basin. Our magnetostratigraphic correlation indicates
440 that the first unconformity (Hiatus 1) spans part of the early C16n.2n, the entire C16r, and a portion of the C17n.1n, most likely beginning in the upper part of C17n.1n. Otherwise, the accumulation rates for magnetozone N4 would be unrealistically high compared to those of the surrounding intervals. This hiatus corresponds to a minimum time interval extending from just before the onset of C16r (~36.6 Ma) to 36.4 Ma. The second unconformity (Hiatus 2) spans part of the early C13n, the whole of C13r, C15n, C15r, and the upper part of the C16n.1n. This corresponds to a minimum interval ranging from 35.6 to 33.8 Ma,
445 including the latest Priabonian and most of the EOT (33.44 to 33.65 Myr, sensu Hutchinson et al., 2021).

The first unconformity is associated with a marked shift in prominent sedimentary facies and is associated with a change of depositional system. Deposits below Hiatus 1 only display one facies association (FA1), which is interpreted as reflecting fine-grained floodplain or alluvial plain deposits (Table 1.; Miall 2010; Leeder 2016). The deposits above Hiatus 1 are dominated by coarser, more energetic, and more pedogenized/carbonated facies grouped in Facies Association 2 (FA2), which is
450 interpreted as a streamflow-dominated alluvial fan/delta with subaqueous portions extending into the lake. This more subaqueous or distal part of the fan-delta is supported by the presence of the facies Smp (See Fig. 4 and Tables 1, 2; Miall 2010; Renaut and Gierlowski-Kordesch 2010).

According to Gülyüz et al. (2013), the local reversal in paleocurrents around that time corresponds to a shift from southward to northward and is interpreted as marking the uplift of the Cicekdagi anticline directly south of our section. This uplift is
455 corroborated by the reworking of nummulitic limestones, starting with Hiatus 1. We thus suggest that the change of sedimentary facies relates to a change in the fluvial network and the regional hydrosystem. During the early parts of the Priabonian, the area was the locus of a southward-oriented, medium-distance drainage network exiting to the southern edge of the Cankiri basin, where the youngest marine deposits are found (Licht et al., 2022). Hiatus 1 marks the uplift of the southern margin of the basin, the disconnection of this river network and the setup of a local, proximal-sourced northward-oriented
460 drainage exiting to a newly formed lacustrine system occupying the Cankiri Basin.

Pedogenesis and carbonate cementation are progressively observed into coarser sediments through the section. At the base, pedogenic features of the Fmp facies (Table 1) are developed within clayey deposits in a floodplain environment. In the upper part of the succession, beginning above Hiatus 1, pedogenesis and carbonate cementation are instead mainly associated with coarser gravity-flow deposits, represented by sandstones of the Smp facies (Table 1). These sandstones accumulated in the



465 distal portions of a fan-delta system, near the lake margin or even within its subaqueous domain. Owing to this transitional position, such deposits were highly sensitive to lake-level fluctuations. The occurrence of well-developed caliches or carbonate-cemented horizons within these sandstones likely indicates phases of lake retreat, during which pedogenesis could develop on exposed surfaces.

470 The second unconformity is not associated with any major change of sedimentary facies but the appearance of dolomite. From the Hiatus 2 onward, almost all of our carbonate-rich sandy facies (Smp) consist predominantly of dolomite. When not related to diagenetic processes, dolomite can precipitate in hypersaline environments such as lagoons or saline lakes (García-Ruiz et al., 2023) depending on local salinity and pH fluctuations (Kim et al., 2023). We thus interpret the appearance of dolomite as reflecting an increase of lake salinity and a shift toward higher evaporation relative to precipitation, where water loss concentrates dissolved salts faster than they are diluted by freshwater inputs (Guo et al., 2023). This interpretation is further 475 supported by the occurrence of Oligocene evaporites in other parts of the Çankırı Basin (Kaymakçı et al., 2003). The synchronicity between the second unconformity and the latest Priabonian and the EOT, a period of documented increase of aridity in many places in Eurasia (Abels et al., 2011; Page et al., 2019; Lettéron et al., 2022; Li et al., 2016; Sun et al., 2020; Semmani et al., 2024), also supports this interpretation. The sedimentary hiatus at the second unconformity was thus likely the combination of a favorable tectonic regime and a period of climate-controlled lake-level drop. Interestingly, the peak of lake 480 retreat starts during the latest Priabonian and covers the EOT, and thus predates the EOGM and the global low of eustatic level (Miller et al., 2008); lake levels increase again during the EOGM. The lake level drop at the second unconformity seems thus uncorrelated with glacio-eustatic levels, and rather related to an earlier, late Priabonian and EOT aridity crisis.

5.3 A first record of the Eocene-Oligocene Transition in Anatolia

485 Our $\Delta 47$ -derived temperatures indicate a drop of ~ 7 °C in soil carbonate growth temperature across the second unconformity, spanning the late Priabonian and the EOT, and persisting through the onset of the EOGM. This temperature drop is similar to what is observed in several other clumped isotope records of the EOT world-wide. A comparable cooling of ~ 7 °C in surface temperatures across the Eocene-Oligocene Transition was documented by Fan et al. (2017) in eastern Wyoming, inferred by 490 clumped isotopes on pedogenic carbonates. In Western Europe, $\Delta 47$ measurements on freshwater gastropods from the Hampshire Basin (England) reveal a ~ 4 – 6 °C decrease (Hren et al., 2013). In northeast Tibet, analyses from the Xining Basin indicate an apparent drop of ~ 20 °C, which has been interpreted as resulting from both a shift in the carbonate growth season and an actual temperature decline, leading to an estimated ~ 9 °C decrease in surface temperatures (Page et al., 2019).

Studies have shown that modern soil carbonates typically form during periods of soil dewatering during warm and dry seasons, 495 and are commonly found in mid-latitude seasonal climate (Methner et al., 2016). This leads to a $\Delta 47$ bias toward Warm Month Mean Temperatures (WMMT) rather than MAT (Methner et al., 2016; Hough et al., 2014; Passey et al., 2010; Peters et al., 2013; Quade et al., 2013). In some instances, particularly under sub-humid climates with alternating wet and dry seasons, carbonate formation may instead reflect values closer to the mean annual temperature (Breecker et al., 2009; Peters et al.,



2013). Under humid tropical monsoonal regimes, the bias can even shift toward recording winter temperatures, more closely
500 reflecting Cold Month Mean Temperatures (CMT; Licht et al., 2022b). We compared our reconstructed surface temperatures
with Eocene temperature estimates from pollen assemblages in Anatolia. There are no paleotemperature estimates for the
Bartonian and Priabonian of central Anatolia, but Raynaud et al. (2025) report paleotemperatures for the Lutetian, stage that
is globally warmer than the later stages of the Eocene (Westerhold et al., 2020). Lutetian Mean Annual Temperatures (MAT)
range from 17.2 to 21.9 °C, while Warm Month Mean Temperatures (WMMT) range from 24.7 to 28.1 °C. Our Δ47-derived
505 temperatures thus likely reflect carbonate growth during the warm season (See Fig. 8). We thus interpret the drop of ~7 °C in
our record as a drop in summer temperatures.

Stable isotope data from pedogenic carbonates reveal no clear change in $\delta^{18}\text{O}$ values across the second unconformity, and a
slight decrease of approximately 0.7‰ is observed in $\delta^{13}\text{C}$ values. Reconstructed $\delta^{18}\text{O}_{\text{water}}$ values exhibit marked variability both
510 before and after the second unconformity, ranging from -1‰ to -4‰. These values contrast with previous reconstructions for
the same region and time interval, which yielded consistently lower values. For example, Licht et al. (2017) reported
 $\delta^{18}\text{O}_{\text{water}}$ values between -5‰ and -7‰ from late Lutetian lacustrine carbonates, while Robert et al. (2025) obtained values of -
5.3‰ to -8‰ from late Lutetian Balkanatolian mammal tooth enamel. The latter are also consistent with modern $\delta^{18}\text{O}$ values
515 of meteoric waters in coastal Mediterranean Anatolia (Schemmel et al., 2013), after applying a ~1‰ correction for differences
in seawater isotopic composition during the Eocene (Tindall et al., 2010), and with Oligocene meteoric water estimates
(Lüdecke et al., 2013). The discrepancy between our reconstructed $\delta^{18}\text{O}_{\text{water}}$ values and those reported in earlier studies may
reflect a proxy-related bias. Reconstructions are expected to capture primary meteoric water signatures, yet the $\delta^{18}\text{O}_{\text{water}}$ is
influenced both by meteoric input and by evaporation. As emphasized by Kelson et al. (2023), evaporation in arid environments
can enrich soil water $\delta^{18}\text{O}_{\text{water}}$ by 1–5‰, even at depths > 40 cm. Such an effect could account for the offset between our
estimates and previous reconstructions, and can explain the great variability in reconstructed soil water $\delta^{18}\text{O}_{\text{water}}$ values.

520 The slight decrease in $\delta^{18}\text{O}_{\text{water}}$ values recorded across the unconformity, from mean values of -1.9‰ to -2.7‰ is thus difficult
to interpret considering the significant imprint of evaporative effects in our record. We note however that a ~7°C air
temperature drop would likely decrease rainwater isotopic composition by ca. -2‰ at these latitudes, and could thus partly
explain this decline (Bowen, 2008).

Our record thus indicates that the Eocene-Oligocene Transition and the EOGM in central Anatolia are associated with summer
525 temperature cooling of ~7°C and an increase of aridity marked first by a temporary lake retreat during the EOT, followed by
a lake rewatering during the EOGM, though marked with a persistent increase in lake salinity compared to the late Priabonian
lake system, as evidenced by the appearance of dolomite beds.



5.4 A Late Eocene Warming?

535 The portion of our section surrounding the first hiatus exhibits more pronounced shifts in isotopic data. Clumped isotope-derived surface temperature estimates reveal a ~9 °C increase beginning with the last paleosol below Hiatus 1, and warm temperatures persist within all paleosols between hiatus 1 and 2. Previous studies (e.g., Bohaty and Zachos, 2003) have documented a ‘Late Eocene Warming’ around ~37–36 Ma seen in benthic foraminiferal records from the Southern Hemisphere. Their reconstructions suggest a ~3–5 °C temperature increase under ice-free conditions. The more recent benthic foraminiferal
540 compilation of Westerhold et al. (2020) dates this warming episode to ~37.5 to ~36.5 Ma. Tremblin et al. (2016) suggest a significant warming of approximately 4 °C in equatorial and North Atlantic regions starting during this time window and lasting until at least 35 Ma, and possibly up to the EOT. The Recent pCO₂ reconstruction of cenCO₂PIP (2023) suggests an increase of pCO₂ during the latest Eocene before the EOT, though the amplitude and chronology of this increase are still poorly constrained. By contrast, Tremblin et al. (2016) suggests that this warming episode could result from a reorganization
545 of ocean circulation in the North Atlantic. Numerous paleoceanographic records in the North Atlantic suggest an onset of a regional subtropical gyre or an early version of the Atlantic meridional overturning circulation (AMOC) around 36 Ma, which could lead to regional warming (Coxall et al., 2018; Liu et al., 2018).

Other records of the late Eocene warming on land are sparse. A recent study made in the Paris Basin records a decrease of δ¹⁸O values on bulk carbonate, also interpreted as a record of the late Eocene Warming during the C16 chron (Le Callonnec et
550 al., 2025). Clumped isotopic data from Tibetan soil carbonates highlight a warming trend across the late Priabonian, culminating between 35 and 34 Myr (Page et al., 2019), and starting after a significant aridification step near the top of chron C17n.1n (Abels et al., 2011), coherent with the beginning of the warming trend observed here.

In our record, this warming is accompanied by a mean δ¹⁸O_{water} increase of 1.7‰, along with enhanced variability. While the mean δ¹⁸O_{water} rises in parallel with temperature, the pronounced variability during the late Eocene suggests increased seasonality
555 and aridity, likely reflecting an increase of evaporative effects in soil carbonates (Kelson et al., 2023). This change is associated with a moderate rise in δ¹³C values of approximately 0.7‰. This shift could be explained by a slight increase in plant water stress, also pointing to a trend toward increased aridity (Cerling and Quade, 1993; Kohn, 2010)

The synchronicity of this apparent increase in temperature and aridity with the first unconformity suggests that it might have partly controlled the chronology of the hiatus. Though the uplift of the basin’s southern margin is likely the primary cause for
560 the discordance, the unconformity might have been enhanced by a base-level drop related to an increase of aridity. Overall, our record highlights an important climatic transition during the early–middle Priabonian within chron C17n.1n and preceding the EOT, marking the onset of an irreversible shift toward more arid conditions, coupled with elevated surface temperatures. This event can be hypothetically attributed to a “late Eocene Warming” impacting Eurasia, though its chronology and origin remain to be more precisely constrained. The subsequent cooling during the EOT brought back clumped isotope temperatures
565 to their earlier, early Priabonian values, but accentuated a long-term trajectory toward increasing aridity.

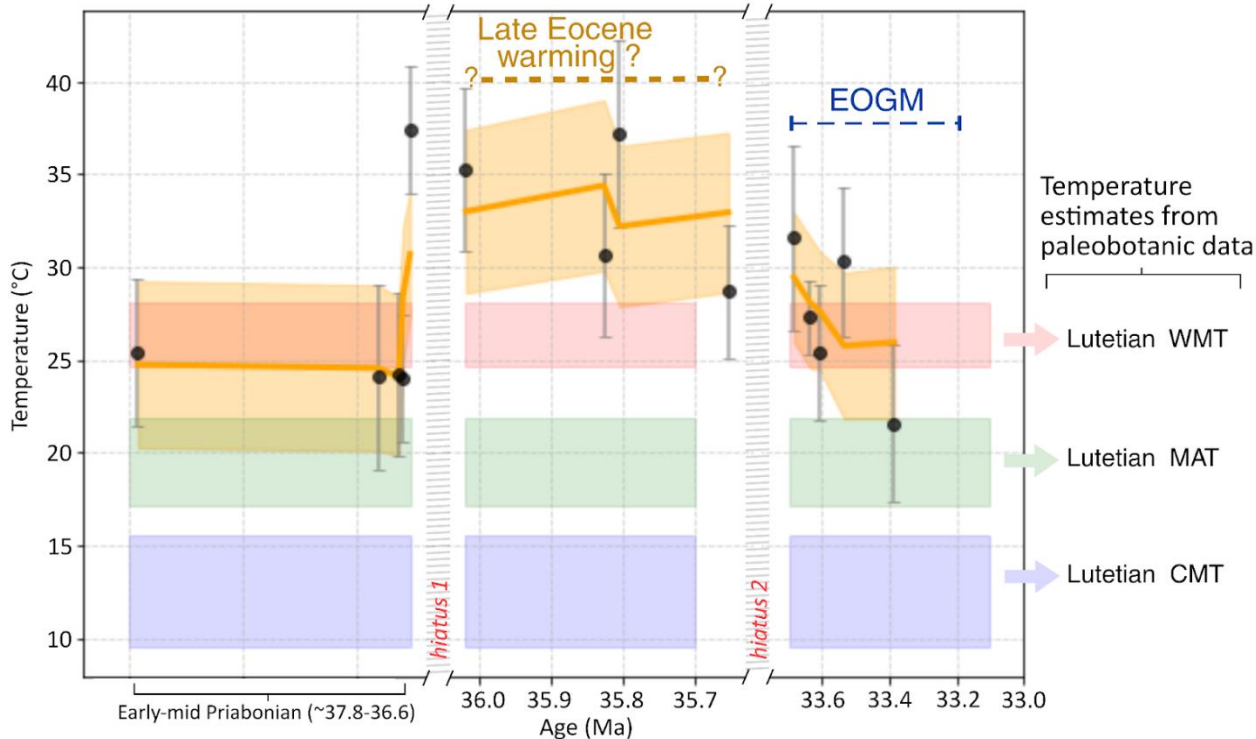


Figure 8: Clumped isotope ($\Delta 47$) paleotemperatures from pedogenic carbonates in the Büyükteflek section (Çicekdagi Basin, Turkey), spanning the Early–Middle Priabonian (~37.8–36.6 Ma) to the Early Rupelian (~33.4 Ma). The orange line shows the moving average; error bars = 1 standard error (SE). Temperature estimates for the Lutetian (48–41 Ma), derived from paleobotanical data reported by Raynaud et al. (2025). (WMT: Warm Month Temperatures; MAT = Mean Annual Temperatures; CMT = Cold Month Temperatures).

575 5.5 Regional climatic response to cooling and implication for Asian terrestrial fauna dispersal

As many previous Eurasian records, our terrestrial section highlights the existence of a profound aridity crisis during the Priabonian, marked by two aridification steps during the middle (Hiatus 1) and latest (Hiatus 2) Priabonian. We show that the first aridification step is associated with a significant warming event, that we attribute to the Late Eocene Warming.

580 This first step likely began sometime between 37 and 36.5 Ma, approximately corresponding to chron C17n.1n. In Western Europe, a comparable aridification phase is observed: Lettéron et al. (2022) describe an increase in aridity within the ASCI (Alès, Saint-Chaptes, and Issirac; France) lake system during the MP17, accompanied by a major turnover in floral



assemblages based on palynological data (Alabouvette et al., 1983; Lettéron et al., 2018). Other records from Central Asia indicate a similar increase in aridity during this interval. Wang et al. (2020) document enhanced aridity in the Tajik Basin, 585 inferred from pedogenic carbonates showing reduced plant-derived soil respiration, correlated with the retreat of the Paratethys Sea during chron C17n.1n. Studies from the Xining Basin likewise record an early phase of aridification occurring during chron C17 (Page et al., 2019; Yang et al., 2022).

The link between this mid Priabonian aridity crisis and the late Eocene warming event is yet difficult to draw. Warming in the North Atlantic related to a proto-AMOC or a regional gyre – the only current explanation for the late Eocene warming – should 590 lead to more regional evaporation and more precipitation on land (Elsworth et al., 2017). It thus cannot explain alone an Eurasian-wide aridity crisis. A tectonically driven Paratethys sea retreat episode in central Asia, as suggested by Wang et al. (2020), could partly explain a regional increase in aridity concomitant with the warmer temperatures of the late Eocene Warming, though its far-field effects up to Balkanatolia and Europe are difficult to predict.

Regardless of its origin, the warming phase observed in our record covers mammalian biohorizons MP18 and MP19 and the 595 first arrival of selected Asia-derived taxa in western Europe, which likely went through Balkanatolia (Metais et al., 2023). This synchronicity suggests that the late Eocene warming could have favored the westward dispersal of several Asia-derived taxa, which were already present on Balkanatolia since the Bartonian (Licht et al., 2022). The environmental stress associated with the warming event and the aridity crisis could have enhanced the decline of endemic Balkanatolian taxa and further favored the penetration of Asia-derived taxa in the region (Raynaud et al., 2025). We note however that MP18 and MP19 times 600 correspond to the peak of endemic mammalian diversity for numerous clades in western Europe (Weppe et al., 2023). The late Eocene warming seems thus to have a different impact in western Europe and Balkanatolia.

The second aridity step is synchronous with the latest Priabonian and EOT and starts in our record at ~35.2 Ma. It is associated with a ~7°C cooling in carbonate growth temperatures leading to the EOGM, which is similar with all other terrestrial clumped isotope records covering the time interval in Eurasia (Page et al., 2019; Hren et al., 2013), and is compatible in amplitude with 605 the rare European paleobotanical records that show some sensitivity to the EOT (Teodoridis and Kvaček, 2015; Suc et al., 2025). It is yet unclear if cooling started with the beginning of the second aridity step associated with the lake retreat at ~35.2 Ma, or, more likely, with the end of the event through the end of the EOT and early EOGM, just before the lake rewatering. Interestingly, the second aridity step predates the EOGM by at least 1.5 Myr, suggesting that its origin is not directly related 610 to the Antarctic glaciation. We suggest that they reflect the hydroclimatic response to an earlier cooling event in the North Atlantic. Indeed, cooling in the North Atlantic seems to have preceded the EOT and to have been heterogeneously spatially and temporally distributed, starting at least 1 Myr before the Eocene Oligocene boundary (Sliwinska et al., 2023). This heterogeneity is so far explained by a complex response of the north Atlantic gyres to decreasing CO₂, which changes gyres' location, strength and structure (Sliwinska et al., 2023). Regardless of its origin, the second aridity step covers mammalian biohorizons MP20 and the onset of biodiversity decline for western European endemic artiodactyls (Weppe et al., 2023). We 615 thus suggest that the environmental stress associated with the second aridity step could have enhanced the decline of western European taxa. It is unclear how this environmental stress impacted Balkanatolian fauna as the paleontological record of the



Priabonian and Rupelian of the area is less complete. However, we note that the last occurrence of Balkanatolian endemic taxa is dated around the EOT (Sanders et al., 2014), suggesting that the local fauna was also impacted. The aridification step and the consecutive EOGM correspond to periods without faunal exchanges between Balkanatolia and western Europe (Mennecart et al., 2021; Metais et al., 2023). This synchronicity is counter-intuitive because the eustatic drop at the EOGM fully connected western Balkanatolia to western Europe (Licht et al., 2022, Montheil et al., 2025). This suggests that this climatic event resulted in the set-up of a persistent environmental barrier in central and southern Europe, blocking the westward penetration of Asia-derived mammals. This paleoenvironmental barrier might have been enhanced by orographic effects on regional precipitation, caused by the nascent Alps (Kocsis et al., 2014).

625

6 Conclusion

Our sedimentological and stable isotope records document two major phases of aridification during the late Eocene. The first, occurring around 37–36.5 Ma, is associated with a marked increase of ~9°C in summer surface temperatures recorded by clumped isotope data, representing the first evidence of the Late Eocene Warming in western Eurasia. The second phase took 630 place during the latest Priabonian, extending through the EOT and into the EOGM, and is characterized by a subsequent decline of ~7°C in summer surface temperatures during the EOGM.

These climatic transitions likely reflect large-scale reorganizations in atmospheric and oceanic circulation in the North Atlantic preceding the EOGM. Such environmental changes may have contributed to the decline of endemic fauna in Balkanatolia and western Europe during the late Eocene. However, the precise chronology and extent of these events require further refinement 635 through integration with additional continental records to strengthen this interpretation.

Data availability

The data and supplementary figures are available as a supplementary material available online.

640 Acknowledgements

This work was supported by the European Research Council (ERC) under the European Union's Horizon 2020 research and innovation programme (grant agreement No. 101043268) to AL. Our geological and paleontological field work has also been supported by grants from the National Science Foundation (EAR 1543684 and 2141115) and the David B. Jones Foundation. We thank Corinne Sonzogni, Anne Alexandre, Mathieu Daeron, Jens Fiebig, Pascal Parmentier, Patricia Rieu et Sylvie de 645 Freitas for their help setting up the Clumped isotope line at CEREGE. We also thank Julien Longerey for helping with sample preparation and imaging at CEREGE, Daniel Borschneck for his help with XRD analysis, Elodie Gazquez for her administrative support and Daniel Robert for his assistance with sample analyses.



Financial support

650 This work has been supported by the European Research Council (ERC) under the European Union's Horizon 2020 research and innovation programme (grant agreement No. 101043268) to AL. Our geological and paleontological field work has also been supported by grants from the National Science Foundation (EAR 1543684 and 2141115) and the David B. Jones Foundation.

Disclaimer

655 Publisher's note: Copernicus Publications remains neutral with regard to jurisdictional claims made in the text, published maps, institutional affiliations, or any other geographical representation in this paper. While Copernicus Publications makes every effort to include appropriate place names, the final responsibility lies with the authors. Views expressed in the text are those of the authors and do not necessarily reflect the views of the publisher

Author contributions

660 PB participated in fieldwork; sample preparation (palaeomagnetism, pedogenic carbonates); data analyses (palaeomagnetism, stable and clumped isotopes); data interpretation; and discussion and writing of the manuscript.
AL participated in fieldwork; clumped isotope data processing; data interpretation; discussion and writing; and supervised the project.

ALJ participated in stable and clumped isotope analyses; clumped isotope data processing; and discussion and writing.

665 LM participated in fieldwork; data interpretation; discussion and writing.
FD participated in data interpretation; discussion and writing.
MK, FO, MSA, GM, BR, and KCB participated in fieldwork; discussion and writing.
DI and PC participated in discussion and writing.

Competing interests

670 The authors declare that they have no conflict of interest.

675



680

685

690

References

Abels, H. A., Dupont-Nivet, G., Xiao, G., Bosboom, R., & Krijgsman, W. (2011). Step-wise change of Asian interior climate preceding the Eocene–Oligocene Transition (EOT). *Palaeogeography, Palaeoclimatology, Palaeoecology*, 299(3-4), 399-412.

695 https://doi.org/10.1016/j.palaeo.2010.11.028

Akgün, F., Akay, E., & Erdoğan, B. (s. d.). Tertiary Terrestrial to Shallow Marine Deposition in Central Anatolia : A Palynological Approach.

Alabouvette, B., Chedhomme, J., Frédet, J.M. and Lartaud, V. (1983) Inventaire des ressources nationales de charbon : lignites du fossé d'Alès-Barjac. Bur. Rech. Géol. Min. Mém., 83, Orléans, 63 pp.

700 Anderson, N. T., Kelson, J. R., Kele, S., Daëron, M., Bonifacie, M., Horita, J., ... & Bergmann, K. D. (2021). A unified clumped isotope thermometer calibration (0.5–1,100 °C) using carbonate-based standardization. *Geophysical Research Letters*, 48(7), e2020GL092069.

Antoine, P.-O., Yans, J., Castillo, A. A., Stutz, N., Abello, M. A., Adnet, S., Custódio, M. A., Benites-Palomino, A., Billet, G., Boivin, M., Herrera, F., Jaramillo, C., Martínez, C., Moreno, F., Navarrete, R. E., Negri, F. R., Parra, F., Pujos, F., Rage, J.-C., ... Marivaux, L. (2021). Biotic community and landscape changes around the Eocene–Oligocene transition at Shapaja, Peruvian Amazonia : Regional or global drivers? *Global and Planetary Change*, 202, 103512.
<https://doi.org/10.1016/j.gloplacha.2021.103512>

Barrier, E., Vrielynck, B., Brouillet, J., Brunet, M., 2018. Paleotectonic reconstruction of the central tethyan realm. Tectono-sedimentary-palinspastic maps from late Permian to Pliocene. CCGM/CGMW, Paris. Atlas of 20.



710 Bernasconi, S. M., Daëron, M., Bergmann, K. D., Bonifacie, M., Meckler, A. N., Affek, H. P., ... & Ziegler, M. (2021). InterCarb: A community effort to improve interlaboratory standardization of the carbonate clumped isotope thermometer using carbonate standards. *Geochemistry, Geophysics, Geosystems*, 22(5), e2020GC009588.

Bohaty, S. M., & Zachos, J. C. (2003). Significant Southern Ocean warming event in the late middle Eocene. *Geology*, 31(11), 1017. <https://doi.org/10.1130/G19800.1>

715 Bowen, G. J. (2008). Spatial analysis of the intra-annual variation of precipitation isotope ratios and its climatological corollaries. *Journal of Geophysical Research: Atmospheres*, 113(D5), 2007JD009295. <https://doi.org/10.1029/2007JD009295>

Breecker, D. O., Sharp, Z. D., & McFadden, L. D. (2009). Seasonal bias in the formation and stable isotopic composition of pedogenic carbonate in modern soils from central New Mexico, USA. *Geological Society of America Bulletin*, 121(3-4), 630-640. <https://doi.org/10.1130/b26413.1>

720 Campbell, C. F., Taylor, M. H., Mueller, M. A., Licht, A., & Ocako, F. (s. d.). The Late Paleogene Çankırı Basin of Türkiye : The geologic record of lithospheric foundering beneath the Central Anatolian Plateau. *Geological Society of America Bulletin*, 136.

Cerling, T. E., & Quade, J. (1993). Stable carbon and oxygen isotopes in soil carbonates. In P. K. Swart, K. C. Lohmann, J. McKenzie, & S. Savin (Eds.), *Climate change in continental isotopic records* (Vol. 78, pp. 217–231). American Geophysical Union

725 Couturier, J., Levard, C., Collin, B., Chaurand, P., Vidal, V., Mathon, O., Duvivier, A., Angeletti, B., Borschneck, D., Rose, J., Pellet-Rostaing, S., & Arrachart, G. (2025). Dissolution of rare earth elements : Exploring the ability of deep eutectic solvents and organic acid solutions, the case of lactic acid. *Separation and Purification Technology*, 366, 132740. <https://doi.org/10.1016/j.seppur.2025.132740>

730 Coxall, H. K., Huck, C. E., Huber, M., Lear, C. H., Legarda-Lisarri, A., O'Regan, M., Sliwinska, K. K., Van De Flierdt, T., De Boer, A. M., Zachos, J. C., & Backman, J. (2018). Export of nutrient rich Northern Component Water preceded early Oligocene Antarctic glaciation. *Nature Geoscience*, 11(3), 190-196. <https://doi.org/10.1038/s41561-018-0069-9>

Daëron, M. (2021). Full propagation of analytical uncertainties in $\Delta 47$ measurements. *Geochemistry, Geophysics, Geosystems*, 22(5), e2020GC009592.

735 Doglioni, C., Busatta, C., Bolis, G., Marianini, L., Zanella, M., 1996. Structural evolution of the eastern Balkans (Bulgaria). *Mar. Pet. Geol.* 13 (2), 225–251.

Elsworth, G., Galbraith, E., Halverson, G., & Yang, S. (2017). Enhanced weathering and CO₂ drawdown caused by latest Eocene strengthening of the Atlantic meridional overturning circulation. *Nature Geoscience*, 10(3), 213-216. <https://doi.org/10.1038/ngeo2888>

740 Eronen, J. T., Janis, C. M., Chamberlain, C. P., & Mulch, A. (2015). Mountain uplift explains differences in Palaeogene patterns of mammalian evolution and extinction between North America and Europe. *Proceedings of the Royal Society B: Biological Sciences*, 282(1809), 20150136. <https://doi.org/10.1098/rspb.2015.0136>



Fan, M., Ayyash, S. A., Tripati, A., Passey, B. H., & Griffith, E. M. (2018). Terrestrial cooling and changes in hydroclimate in the continental interior of the United States across the Eocene-Oligocene boundary. *GSA Bulletin*, 130(7-8), 1073-1084.

745 <https://doi.org/10.1130/b31732.1>

Fiebig, J., Bernecker, M., Meijer, N., Methner, K., Staudigel, P. T., Davies, A. J., ... & Petersen, S. V. (2024). Carbonate clumped isotope values compromised by nitrate-derived NO₂ interferent. *Chemical Geology*, 670, 122382.

García-Ruiz, J. M. (2023). A fluctuating solution to the dolomite problem. *Science*, 382(6673), 883-884.
<https://doi.org/10.1126/science.adl1734>

750 Gradstein, F. M., Ogg, J. G., Schmitz, M. D., & Ogg, G. M. (Eds.). (2020). *Geologic time scale 2020*. Elsevier.

Gülyüz, E., Kaymakci, N., Meijers, M. J. M., Van Hinsbergen, D. J. J., Lefebvre, C., Vissers, R. L. M., Hendriks, B. W. H., & Peynircioğlu, A. A. (2013). Late Eocene evolution of the Çiçekdağı Basin (central Turkey) : Syn-sedimentary compression during microcontinent-continent collision in central Anatolia. *Tectonophysics*, 602, 286-299.
<https://doi.org/10.1016/j.tecto.2012.07.003>

755 Guo, P., Wen, H., Li, C., He, H., & Sánchez-Román, M. (2023). Lacustrine dolomite in deep time : What really matters in early dolomite formation and accumulation? *Earth-Science Reviews*, 246, 104575.
<https://doi.org/10.1016/j.earscirev.2023.104575>

Gürer, D., Van Hinsbergen, D. J. J., Matenco, L., Corfu, F., & Casella, A. (2016). Kinematics of a former oceanic plate of the Neotethys revealed by deformation in the Ulukışla basin (Turkey). *Tectonics*, 35(10), 2385-2416.

760 <https://doi.org/10.1002/2016TC004206>

Hough, B. G., Fan, M., & Passey, B. H. (2014). Calibration of the clumped isotope geothermometer in soil carbonate in Wyoming and Nebraska, USA : Implications for paleoelevation and paleoclimate reconstruction. *Earth and Planetary Science Letters*, 391, 110-120. <https://doi.org/10.1016/j.epsl.2014.01.008>

765 Hren, M. T., Sheldon, N. D., Grimes, S. T., Collinson, M. E., Hooker, J. J., Bugler, M., & Lohmann, K. C. (2013). Terrestrial cooling in Northern Europe during the Eocene–Oligocene transition. *Proceedings of the National Academy of Sciences*, 110(19), 7562-7567. <https://doi.org/10.1073/pnas.1210930110>

Hutchinson, D. K., Coxall, H. K., Lunt, D. J., Steinthorsdottir, M., de Boer, A. M., Baatsen, M., von der Heydt, A., Huber, M., Kennedy-Asser, A. T., Kunzmann, L., Ladant, J.-B., Lear, C. H., Moraweck, K., Pearson, P. N., Piga, E., Pound, M. J., Salzmann, U., Scher, H. D., Sijp, W. P., ... Zhang, Z. (2021). The Eocene–Oligocene transition : A review of marine and terrestrial proxy data, models and model–data comparisons. *Climate of the Past*, 17(1), 269-315. <https://doi.org/10.5194/cp-17-269-2021>

Judd, E. J., Tierney, J. E., Lunt, D. J., Montañez, I. P., Huber, B. T., Wing, S. L., & Valdes, P. J. (2024). A 485-million-year history of Earth's surface temperature. *Science*, 385(6715), eadk3705. <https://doi.org/10.1126/science.adk3705>



Katz, M. E., Miller, K. G., Wright, J. D., Wade, B. S., Browning, J. V., Cramer, B. S., & Rosenthal, Y. (2008). Stepwise transition from the Eocene greenhouse to the Oligocene icehouse. *Nature Geoscience*, 1(5), 329-334. <https://doi.org/10.1038/ngeo179>

Kaymakci, N., White, S. H., & Vandijk, P. M. (2003). Kinematic and structural development of the Çankiri Basin (Central Anatolia, Turkey): A paleostress inversion study. *Tectonophysics*, 364(1-2), 85-113. [https://doi.org/10.1016/S0040-1951\(03\)00043-X](https://doi.org/10.1016/S0040-1951(03)00043-X)

Kelson, J. R., Huth, T. E., Passey, B. H., Levin, N. E., Petersen, S. V., Ballato, P., Beverly, E. J., Breecker, D. O., Hoke, G. D., Hudson, A. M., Ji, H., Licht, A., Oerter, E. J., & Quade, J. (2023). Triple oxygen isotope compositions of globally distributed soil carbonates record widespread evaporation of soil waters. *Geochimica et Cosmochimica Acta*, 355, 138-160. <https://doi.org/10.1016/j.gca.2023.06.034>

Kent-Corson, M. L., Ritts, B. D., Zhuang, G., Bovet, P. M., Graham, S. A., & Page Chamberlain, C. (2009). Stable isotopic constraints on the tectonic, topographic, and climatic evolution of the northern margin of the Tibetan Plateau. *Earth and Planetary Science Letters*, 282(1-4), 158-166. <https://doi.org/10.1016/j.epsl.2009.03.011>

Kim, J., Kimura, Y., Puchala, B., Yamazaki, T., Becker, U., & Sun, W. (2023). Dissolution enables dolomite crystal growth near ambient conditions. *Science*, 382(6673), 915-920. <https://doi.org/10.1126/science.adl3690>

Kocsis, L., Ozsvárt, P., Becker, D., Ziegler, R., Scherler, L., & Codrea, V. (2014). Orogeny forced terrestrial climate variation during the late Eocene–early Oligocene in Europe. *Geology*, 42(8), 727-730. <https://doi.org/10.1130/G35673.1>

Kohn, M. J. (2010). Carbon isotope compositions of terrestrial C3 plants as indicators of (paleo) ecology and (paleo) climate. *Proceedings of the National Academy of Sciences*, 107(46), 19691-19695.

Kohn, M. J., Strömborg, C. A. E., Madden, R. H., Dunn, R. E., Evans, S., Palacios, A., & Carlini, A. A. (2015). Quasi-static Eocene–Oligocene climate in Patagonia promotes slow faunal evolution and mid-Cenozoic global cooling. *Palaeogeography, Palaeoclimatology, Palaeoecology*, 435, 24-37. <https://doi.org/10.1016/j.palaeo.2015.05.028>

Laurence Le Callonnec, Châteauneuf, J.-J., Renard, M., Zuddas, P., Emmanuel, L., & Riveline, J. (2025). New Data on the Recording of Global Climatic Events at the Eocene–Oligocene Transition in the Sediments of the Paris Basin (Cormeilles-en-Parisis Section). *Stratigraphy and Geological Correlation*, 33(2), 257-277. <https://doi.org/10.1134/S0869593824700357>

Lefebvre, C., Meijers, M. J. M., Kaymakci, N., Peynircioğlu, A., Langereis, C. G., & Van Hinsbergen, D. J. J. (2013). Reconstructing the geometry of central Anatolia during the late Cretaceous : Large-scale Cenozoic rotations and deformation between the Pontides and Taurides. *Earth and Planetary Science Letters*, 366, 83-98. <https://doi.org/10.1016/j.epsl.2013.01.003>

Lettéron, A., Fournier, F., Hamon, Y., Villier, L., Margerel, J.-P., Bouche, A., Feist, M., & Joseph, P. (2017). Multi-proxy paleoenvironmental reconstruction of saline lake carbonates : Paleoclimatic and paleogeographic implications (Priabonian-Rupelian, Issirac Basin, SE France). *Sedimentary Geology*, 358, 97-120. <https://doi.org/10.1016/j.sedgeo.2017.07.006>



Lettéron, A., Hamon, Y., Fournier, F., Demory, F., Séranne, M., & Joseph, P. (2022). Stratigraphic architecture of a saline lake system : From lake depocentre (Alès Basin) to margins (Saint-Chaptes and Issirac basins), Eocene–Oligocene transition, south-east France. *Sedimentology*, 69(2), 651-695. <https://doi.org/10.1111/sed.12920>

Lettéron, A., Hamon, Y., Fournier, F., Séranne, M., Pellenard, P., & Joseph, P. (2018). Reconstruction of a saline, lacustrine carbonate system (Priabonian, St-Chaptes Basin, SE France) : Depositional models, paleogeographic and paleoclimatic implications. *Sedimentary Geology*, 367, 20-47. <https://doi.org/10.1016/j.sedgeo.2017.12.023>

Li, B., Sun, D., Wang, X., Zhang, Y., Hu, W., Wang, F., Li, Z., Ma, Z., & Liang, B. (2016). $\delta^{18}\text{O}$ and $\delta^{13}\text{C}$ records from a Cenozoic sedimentary sequence in the Lanzhou Basin, Northwestern China : Implications for palaeoenvironmental and palaeoecological changes. *Journal of Asian Earth Sciences*, 125, 22-36. <https://doi.org/10.1016/j.jseaes.2016.05.010>

Li, Q., Zhang, Y., Dong, L., & Guo, Z. (2018). Oligocene syndepositional lacustrine dolomite : A study from the southern Junggar Basin, NW China. *Palaeogeography, Palaeoclimatology, Palaeoecology*, 503, 69-80. <https://doi.org/10.1016/j.palaeo.2018.04.004>

Li, S., & Guan, P. (2023). Advances in carbon and oxygen isotopes and clumped isotope of lacustrine carbonates. *Acta Scientiarum Naturalium Universitatis Pekinensis*, 59(6), 1052-1068.

Licht, A., Coster, P., Ocakoğlu, F., Campbell, C., Métais, G., Mulch, A., Taylor, M., Kappelman, J., & Beard, K. C. (2017). Tectono-stratigraphy of the Orhaniye Basin, Turkey : Implications for collision chronology and Paleogene biogeography of central Anatolia. *Journal of Asian Earth Sciences*, 143, 45-58. <https://doi.org/10.1016/j.jseaes.2017.03.033>

Licht, A., Kelson, J., Bergel, S., Schauer, A., Petersen, S. V., Capirala, A., Huntington, K. W., Dupont-Nivet, G., Win, Z., & Aung, D. W. (2022). Dynamics of Pedogenic Carbonate Growth in the Tropical Domain of Myanmar. *Geochemistry, Geophysics, Geosystems*, 23(7), e2021GC009929. <https://doi.org/10.1029/2021GC009929>

Licht, A., Métais, G., Coster, P., İbilioğlu, D., Ocakoğlu, F., Westerweel, J., Mueller, M., Campbell, C., Mattingly, S., Wood, M. C., & Beard, K. C. (2022). Balkanatolia : The insular mammalian biogeographic province that partly paved the way to the Grande Coupure. *Earth-Science Reviews*, 226, 103929. <https://doi.org/10.1016/j.earscirev.2022.103929>

Liu, Z., Huang, C., Algeo, T. J., Liu, H., Hao, Y., Du, X., Lu, Y., Chen, P., Guo, L., & Peng, L. (2018). High-resolution astrochronological record for the Paleocene-Oligocene (66–23 Ma) from the rapidly subsiding Bohai Bay Basin, northeastern China. *Palaeogeography, Palaeoclimatology, Palaeoecology*, 510, 78-92. <https://doi.org/10.1016/j.palaeo.2017.10.030>

Lüdecke, T. (2013). Stable isotope-based reconstruction of Oligo-Miocene paleoenvironment and paleohydrology of Central Anatolian lake basins (Turkey). *TURKISH JOURNAL OF EARTH SCIENCES*. <https://doi.org/10.3906/yer-1207-11>

Meijer, N., Methner, K., Seymour, N. M., Bernecker, M., Fiebig, J., Voigt, S., Chamberlain, C. P., & Mulch, A. (2025). Oligocene cooling in the North American cordillera (SW Montana, USA) revealed by dual clumped isotope thermometry. *Earth and Planetary Science Letters*, 671, 119618. <https://doi.org/10.1016/j.epsl.2025.119618>

Meng, J., & McKenna, M. C. (1998). Faunal turnovers of Palaeogene mammals from the Mongolian Plateau. *Nature*, 394(6691), 364-367. <https://doi.org/10.1038/28603>



840 Mennecart, B., Aiglstorfer, M., Li, Y., Li, C., & Wang, S. (2021). Ruminants reveal Eocene Asiatic palaeobiogeographical provinces as the origin of diachronous mammalian Oligocene dispersals into Europe. *Scientific Reports*, 11(1), 17710. <https://doi.org/10.1038/s41598-021-96221-x>

Métais, G., Coster, P., Licht, A., Ocakoğlu, F., & Beard, K. C. (2023). Additions to the late Eocene Süngülü mammal fauna in Easternmost Anatolia and the Eocene-Oligocene transition at the periphery of Balkanatolia. *Comptes Rendus Palevol*, 35. <https://doi.org/10.5852/cr-palevol2023v22a35>

845 Métais, G., Coster, P. M., Kappelman, J. R., Licht, A., Ocakoğlu, F., Taylor, M. H., & Beard, K. C. (2018a). Eocene metatherians from Anatolia illuminate the assembly of an island fauna during Deep Time. *PLOS ONE*, 13(11), e0206181. <https://doi.org/10.1371/journal.pone.0206181>

Métais, G., Coster, P. M., Kappelman, J. R., Licht, A., Ocakoğlu, F., Taylor, M. H., & Beard, K. C. (2018b). Eocene metatherians from Anatolia illuminate the assembly of an island fauna during Deep Time. *PLOS ONE*, 13(11), e0206181. <https://doi.org/10.1371/journal.pone.0206181>

850 Methner, K., Mulch, A., Fiebig, J., Wacker, U., Gerdes, A., Graham, S. A., & Chamberlain, C. P. (2016). Rapid Middle Eocene temperature change in western North America. *Earth and Planetary Science Letters*, 450, 132-139. <https://doi.org/10.1016/j.epsl.2016.05.053>

Miall AD. 2010. Alluvial deposits. *Facies models* 4: 105–138.

855 Miller, K. G., Wright, J. D., and Fairbanks, R. G.: Unlocking the Ice House: Oligocene-Miocene oxygen isotopes, eustasy, and margin erosion, *J. Geophys. Res.-Sol. Ea.*, 96, 6829–6848, <https://doi.org/10.1029/90JB02015>, 1991.

Miller, K. G., Browning, J. V., Aubry, M.-P., Wade, B. S., Katz, M. E., Kulpeck, A. A., & Wright, J. D. (2008). Eocene-Oligocene global climate and sea-level changes : St. Stephens Quarry, Alabama. *Geological Society of America Bulletin*, 120(1-2), 34-53. <https://doi.org/10.1130/B26105.1>

860 Montheil, L., Licht, A., İbilioglu, D., Botté, P., Ocakoğlu, F., Demory, F., Ruffet, G., Guihou, A., Kaya, M., Raynaud, B., Akkiraz, M. S., Deschamps, P., Métais, G., Coster, P., & Beard, K. C. (2025). Updating the timeline of faunal endemism in Balkanatolia, the biogeographic province connecting Europe, Asia and Africa. *Journal of Asian Earth Sciences*, 290, 106661. <https://doi.org/10.1016/j.jseas.2025.106661>

Montheil, L., Licht, A., Beard, K. C., Métais, G., Coster, P., Vaes, B., Donnadieu, Y., Pineau, E., Husson, L., & Dupont-Nivet, G. (2025). Across ancient oceans: Eocene dispersal routes of Asian terrestrial mammals to Europe, Afro-Arabia and South America. *Earth-Science Reviews*. <https://doi.org/10.1016/j.earscirev.2025.105352>

Mueller, M. A., Licht, A., Campbell, C., Ocakoğlu, F., Akşit, G. G., Métais, G., Coster, P. M. C., Beard, K. C., & Taylor, M. H. (2022). Sedimentary Provenance From the Evolving Forearc-to-Foreland Central Sakarya Basin, Western Anatolia Reveals Multi-Phase Intercontinental Collision. *Geochemistry, Geophysics, Geosystems*, 23(3), e2021GC010232. <https://doi.org/10.1029/2021GC010232>



Page, M., Licht, A., Dupont-Nivet, G., Meijer, N., Barbolini, N., Hoorn, C., Schauer, A., Huntington, K., Bajnai, D., Fiebig, J., Mulch, A., & Guo, Z. (2019). Synchronous cooling and decline in monsoonal rainfall in northeastern Tibet during the fall into the Oligocene icehouse. *Geology*, 47(3), 203-206. <https://doi.org/10.1130/G45480.1>

Palcu, D. V., & Krijgsman, W. (2023). The dire straits of Paratethys : Gateways to the anoxic giant of Eurasia. *Geological Society, London, Special Publications*, 523(1), 111-139. <https://doi.org/10.1144/SP523-2021-73>

875 Passey, B. H., Levin, N. E., Cerling, T. E., Brown, F. H., & Eiler, J. M. (2010). High-temperature environments of human evolution in East Africa based on bond ordering in paleosol carbonates. *Proceedings of the National Academy of Sciences*, 107(25), 11245-11249. <https://doi.org/10.1073/pnas.1001824107>

Peters, N. A., Huntington, K. W., & Hoke, G. D. (2013). Hot or not? Impact of seasonally variable soil carbonate formation on paleotemperature and O-isotope records from clumped isotope thermometry. *Earth and Planetary Science Letters*, 361, 208-218. <https://doi.org/10.1016/j.epsl.2012.10.024>

880 Popov, S.V., Rögl, F., Rozanov, A.Y., Steininger, F.F., Shcherba, I.G., Kovac, M., 2004. Lithological-Paleogeographic Maps of Paratethys-10 Maps Late Eocene to Pliocene.

Pound, M. J., & Salzmann, U. (2017). Heterogeneity in global vegetation and terrestrial climate change during the late Eocene to early Oligocene transition. *Scientific Reports*, 7(1), 43386. <https://doi.org/10.1038/srep43386>

Quade, J., Eiler, J., Daëron, M., & Achyuthan, H. (2013). The clumped isotope geothermometer in soil and paleosol carbonate. *Geochimica et Cosmochimica Acta*, 105, 92-107. <https://doi.org/10.1016/j.gca.2012.11.031>

885 Raynaud, B., Akkiraz, M. S., Boura, A., Hoorn, C., Gibson, M., Giobbini, A., Botté, P., Montheil, L., Kaya, M., Ocakoğlu, F., Ibilioglu, D., Métais, G., Beard, K. C., Coster, P., & Licht, A. Lutetian swamp-freshwater palynoflora from Bultu-Zile (central Anatolia, Türkiye): implications for Eocene ecosystems of Balkanatolia. *Journal of Asian Earth Sciences* (in Review).

Renaut RW, Gierlowski-Kordesch EH, 2010. Lakes. Facies models 4: 541–575.

Robert, D., M.A. Birmingham, A. Licht, A. Olcott, A.-L. Jourdan, A. Guihou, Marina Suarez , R. Amiot, A. Vinçon-Laugier, P. Botté, F. Ocakoğlu, L. Montheil, M. Kaya, B. Raynaud, M.S. Akkiraz, P. Deschamps, G. Métais, P. Coster, & K.C. Beard. Isotopic Constraints on the Ecology and Dispersal of Lutetian Embritopods from Balkanatolia. *Palaios* (in review).

895 Sanders, W. J., Nemec, W., Aldinucci, M., Janbu, N. E., & Ghinassi, M. (2014). Latest evidence of *Palaeoamasia* (Mammalia, Embritopoda) in Turkish Anatolia. *Journal of Vertebrate Paleontology*, 34(5), 1155-1164. <https://doi.org/10.1080/02724634.2014.850430>

Schemmel, F., Mikes, T., Rojay, B., & Mulch, A. (2013). The impact of topography on isotopes in precipitation across the Central Anatolian Plateau (Turkey). *American Journal of Science*, 313(2), 61-80. <https://doi.org/10.2475/02.2013.01>

900 Semmani, N., Fournier, F., Suc, J.-P., Fauquette, S., Séranne, M., Léonide, P., Marié, L., & Borgomaner, J. (2024). Continental depositional record of climate and tectonic evolution around the Eocene-Oligocene transition in southeast France : Perspectives from the Vistrenque Basin (Camargue). *BSGF - Earth Sciences Bulletin*, 195, 8. <https://doi.org/10.1051/bsgf/2024005>



Sheldon, N. D. (2009). Nonmarine records of climatic change across the Eocene-Oligocene transition. In C. Koeberl & A. Montanari, *The Late Eocene Earth—Hothouse, Icehouse, and Impacts*. Geological Society of America.
905 https://doi.org/10.1130/2009.2452(15)

Sheldon, N. D., Costa, E., Cabrera, L., & Garcés, M. (2012). Continental Climatic and Weathering Response to the Eocene-Oligocene Transition. *The Journal of Geology*, 120(2), 227-236. <https://doi.org/10.1086/663984>

Śliwińska, K. K., Coxall, H. K., Hutchinson, D. K., Liebrand, D., Schouten, S., & De Boer, A. M. (2023). Sea surface temperature evolution of the North Atlantic Ocean across the Eocene–Oligocene transition. *Climate of the Past*, 19(1), 910 123-140. <https://doi.org/10.5194/cp-19-123-2023>

Suc, J.-P., Fauquette, S., Popescu, S.-M., Melinte-Dobrinescu, M. C., Huet, B., Sorrel, P., Semmani, N., Fournier, F., Bessedik, M., Zheng, Z., Truc, G., Ferry, S., Rubino, J.-L., Girard, V., & Séranne, M. (2025). Late Eocene to Early Miocene environments, vegetation and climate in Southeastern France documented by palynology. *Palaeogeography, Palaeoclimatology, Palaeoecology*, 659, 112625. <https://doi.org/10.1016/j.palaeo.2024.112625>

915 Sun, Y., Liu, J., Liang, Y., Ji, J., Liu, W., Aitchison, J. C., Sun, J., Lu, J., Song, B., Xu, Y., Zhang, K., & Liu, Z. (2020). Cenozoic moisture fluctuations on the northeastern Tibetan Plateau and association with global climatic conditions. *Journal of Asian Earth Sciences*, 200, 104490. <https://doi.org/10.1016/j.jseaes.2020.104490>

Tardif, D., Toumoulin, A., Fluteau, F., Donnadieu, Y., Le Hir, G., Barbolini, N., Licht, A., Ladant, J.-B., Sepulchre, P., Viovy, N., Hoorn, C., & Dupont-Nivet, G. (2021). Orbital variations as a major driver of climate and biome distribution during the 920 greenhouse to icehouse transition. *Science Advances*, 7(43), eabh2819. <https://doi.org/10.1126/sciadv.abh2819>

Teodoridis, V., & Kvaček, Z. (2015). Palaeoenvironmental evaluation of Cainozoic plant assemblages from the Bohemian Massif (Czech Republic) and adjacent Germany. *Bulletin of Geosciences*, 695-720. <https://doi.org/10.3140/bull.geosci.1553>

The Cenozoic CO Proxy Integration Project (CenCOPIP) Consortium*†, Hönisch, B., Royer, D. L., Breecker, D. O., Polissar, P. J., Bowen, G. J., Henehan, M. J., Cui, Y., Steinthorsdottir, M., McElwain, J. C., Kohn, M. J., Pearson, A., Phelps, S. R., 925 Uno, K. T., Ridgwell, A., Anagnostou, E., Austermann, J., Badger, M. P. S., Barclay, R. S., ... Zhang, L. (2023). Toward a Cenozoic history of atmospheric CO₂. *Science*, 382(6675), eadi5177. <https://doi.org/10.1126/science.adi5177>

Tindall, J., Flecker, R., Valdes, P., Schmidt, D. N., Markwick, P., & Harris, J. (2010). Modelling the oxygen isotope distribution of ancient seawater using a coupled ocean–atmosphere GCM: Implications for reconstructing early Eocene climate. *Earth and Planetary Science Letters*, 292(3-4), 265-273. <https://doi.org/10.1016/j.epsl.2009.12.049>

930 Toumoulin, A., Tardif, D., Donnadieu, Y., Licht, A., Ladant, J.-B., Kunzmann, L., & Dupont-Nivet, G. (2022). Evolution of continental temperature seasonality from the Eocene greenhouse to the Oligocene icehouse –a model–data comparison. *Climate of the Past*, 18(2), 341-362. <https://doi.org/10.5194/cp-18-341-2022>

Tremblin, M., Hermoso, M., & Minoletti, F. (2016). Equatorial heat accumulation as a long-term trigger of permanent Antarctic ice sheets during the Cenozoic. *Proceedings of the National Academy of Sciences*, 113(42), 11782-11787.

935 https://doi.org/10.1073/pnas.1608100113



Van Hinsbergen, D. J. J., Kaymakci, N., Spakman, W., & Torsvik, T. H. (2010). Reconciling the geological history of western Turkey with plate circuits and mantle tomography. *Earth and Planetary Science Letters*, 297(3-4), 674-686. <https://doi.org/10.1016/j.epsl.2010.07.024>

Van Hinsbergen, D. J. J., Maffione, M., Plunder, A., Kaymakci, N., Ganerød, M., Hendriks, B. W. H., Corfu, F., Gürer, D.,
940 De Gelder, G. I. N. O., Peters, K., McPhee, P. J., Brouwer, F. M., Advokaat, E. L., & Vissers, R. L. M. (2016). Tectonic evolution and paleogeography of the Kırşehir Block and the Central Anatolian Ophiolites, Turkey : TECTONIC EVOLUTION OF CENTRAL ANATOLIA. *Tectonics*, 35(4), 983-1014. <https://doi.org/10.1002/2015TC004018>

Van Hinsbergen, D. J. J., Torsvik, T. H., Schmid, S. M., Maťenco, L. C., Maffione, M., Vissers, R. L. M., Gürer, D., & Spakman, W. (2020). Orogenic architecture of the Mediterranean region and kinematic reconstruction of its tectonic evolution
945 since the Triassic. *Gondwana Research*, 81, 79-229. <https://doi.org/10.1016/j.gr.2019.07.009>

Wang, X., Carrapa, B., Sun, Y., Dettman, D. L., Chapman, J. B., Caves Rugenstein, J. K., Clementz, M. T., DeCelles, P. G.,
Wang, M., Chen, J., Quade, J., Wang, F., Li, Z., Oimuhammadzoda, I., Gadoev, M., Lohmann, G., Zhang, X., & Chen, F.
(2020). The role of the westerlies and orography in Asian hydroclimate since the late Oligocene. *Geology*, 48(7), 728-732.
<https://doi.org/10.1130/G47400.1>

950 Weppe, R., Condamine, F. L., Guinot, G., Maugoust, J., & Orliac, M. J. (2023). Drivers of the artiodactyl turnover in insular western Europe at the Eocene–Oligocene Transition. *Proceedings of the National Academy of Sciences*, 120(52), e2309945120. <https://doi.org/10.1073/pnas.2309945120>

Westerhold, T., Marwan, N., Drury, A. J., Liebrand, D., Agnini, C., Anagnostou, E., Barnet, J. S. K., Bohaty, S. M., De
Vleeschouwer, D., Florindo, F., Frederichs, T., Hodell, D. A., Holbourn, A. E., Kroon, D., Lauretano, V., Littler, K., Lourens,
955 L. J., Lyle, M., Pälike, H., ... Zachos, J. C. (2020). An astronomically dated record of Earth's climate and its predictability over the last 66 million years. *Science*, 369(6509), 1383-1387. <https://doi.org/10.1126/science.aba6853>

Yang, Y., Fang, X., Han, W., Wang, Y., & Galy, A. (2022). Terrestrial carbonate oxygen isotopes constraints on the interplay between westerlies and monsoonal rains modulating the Cenozoic climate on the northeastern Tibetan Plateau. *Palaeogeography, Palaeoclimatology, Palaeoecology*, 608, 111289. <https://doi.org/10.1016/j.palaeo.2022.111289>

960 Zachos, J. C., Quinn, T. M., & Salamy, K. A. (1996). High-resolution (10^4 years) deep-sea foraminiferal stable isotope records of the Eocene-Oligocene climate transition. *Paleoceanography*, 11(3), 251-266. <https://doi.org/10.1029/96PA00571>